Materials Today Bio 29 (2024) 101299

Contents lists available at ScienceDirect

Materials Today Bio

journal homepage: www.journals.elsevier.com/materials-today-bio

Intelligent nanocatalyst mediated lysosomal ablation pathway to coordinate the amplification of tumor treatment

Mingliang Pei [a,c,1,*], Xin Guan [b,1], De Zhao [e,1], Fan Yang [c], Yun Dong [d], Manxiu Huai [f], Wensong Ge [f], Xiaodong Hou [a], Wenfeng Chu [f], Kai Wang [d], Jie Chen [d,**], Huixiong Xu [b,***]

[a] Department of Medical Ultrasound and Center of Minimally Invasive Treatment for Tumor, Shanghai Tenth People's Hospital, School of Medicine, Tongji University, No. 301 Yan-chang-zhong Road, Shanghai, 200072, PR China
[b] Department of Ultrasound, Zhongshan Hospital, Institute of Ultrasound in Medicine and Engineering, Fudan University, Shanghai, 200032, PR China
[c] Department of Orthopaedics, Shanghai Key Laboratory for Prevention and Treatment of Bone and Joint Diseases, Shanghai Institute of Traumatology and Orthopaedics, Ruijin Hospital, Shanghai Jiao Tong University School of Medicine, Shanghai, 200025, PR China
[d] Shanghai Chest Hospital, Shanghai Jiao Tong University School of Medicine, No.241 West Huaihai Road, Shanghai, 200030, PR China
[e] Key Laboratory for Translational Research and Innovative Therapeutics of Gastrointestinal Oncology, Hongqiao International Institute of Medicine, Department of Gastroenterology, Shanghai Tongren Hospital, Shanghai Jiao Tong University School of Medicine, Shanghai, 200336, PR China
[f] Department of Gastroenterology, Xinhua Hospital, Shanghai Jiaotong University, School of Medicine. No. 1665 Kongjiang Road, Shanghai, 200092, PR China

ARTICLE INFO

Keywords:
pH-unlocked $^1O_2$ generation
Tumor therapy
Lysosomal damnification
Programmed ROS strategy

ABSTRACT

The production of reactive oxygen species (ROS) is susceptible to external excitation or insufficient supply of related participants (*e.g.*, hydrogen peroxide (H_2O_2) and sensitizer), liming ROS-driven tumor treatment. Additionally, the lysosomal retention effect severely hinders the utilization of ROS-based nanosystems and severely restricted the therapeutic effect of tumors. Therefore, first reported herein an intelligent nanocatalyst, TCPP-Cu@MnO_x ($(Mn^{II})_1(Mn^{III})_{2.1}(Mn^{IV})_{2.6}O_{9.35}$), and proposed a programmed ROS amplification strategy to treat tumors. Initially, the acidity-unlocked nanocatalyst was voluntarily triggered to generate abundant singlet oxygen ($^1O_2$) to mediate acid lysosomal ablation to assist nanocatalyst escape and partially induce lysosomal death, a stage known as lysosome-driven therapy. More unexpectedly, the high-yielding production of $^1O_2$ in acid condition (pH 5.0) was showed compared to neutral media (pH 7.4), with a difference of about 204 times between the two. Subsequently, the escaping nanocatalyst further activated H_2O_2-mediated $^1O_2$ and hydroxyl radical (•OH) generation and glutathione (GSH) consumption for further accentuation tumor therapy efficiency, which is based on the Fenton-like reaction and Russell reaction mechanisms. Therefore, in this system, a program-activatable TCPP-Cu@MnO_x nanocatalyst, was proposed to efficiently destruct organelle-lysosome *via* $^1O_2$ inducing, and stimulated H_2O_2 conversion into highly toxic $^1O_2$ and •OH in cytoplasm, constituting an attractive method to overcome limitations of current ROS treatment.

1. Introduction

At present, the strategy of effectively and conveniently inducting the production of reactive oxygen species (ROS), as a novel and unique treatment pattern, has made great progress in the treatment of tumors [1,2]. Compared to clinical standardized treatment options, *e.g.,* chemotherapy, surgical resection and radiotherapy, ROS-mediated tumor therapy is widely favored owing to its unique characteristics such as high efficiency, low cytotoxicity to normal cells, and negligible multidrug resistance to induced tumor cells. Recently, including chemodnamic therapy (CDT) [3,4], photodynamic (PDT) [5] and sonodynamic therapy (SDT) [6,7] *etc.*, these emerging strategies on ROS-associated cancer therapy have made significant progress. However, many inevitable problems seriously hinder their application, especially in internal/external energy-triggered the production of ROS to ablate tumors. For example, hydrogen peroxide (H_2O_2) mediated-CDT

* Corresponding author.
** Corresponding author.
*** Corresponding author.
E-mail addresses: pei1991@sjtu.edu.cn (M. Pei), snoopy_cj@126.com (J. Chen), xuhuixiong@126.com (H. Xu).
[1] The authors contributed equally to this work.

https://doi.org/10.1016/j.mtbio.2024.101299
Received 30 July 2024; Received in revised form 30 September 2024; Accepted 14 October 2024
Available online 16 October 2024

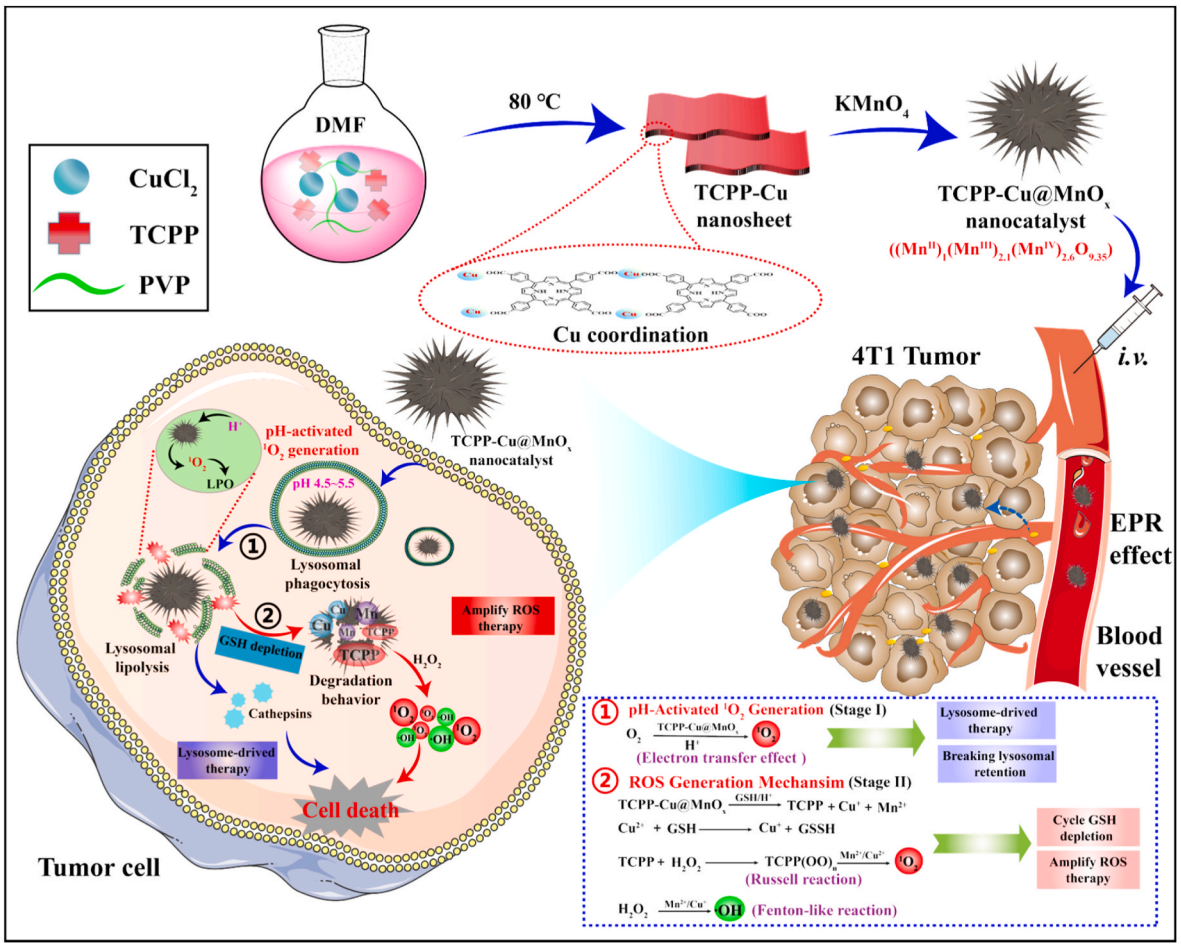

Fig. 1. Schematic illustration of fabrication and antitumor effect of intelligent TCPP-Cu@MnO_x nanocatalyst. Synthetic procedure for TCPP-Cu@MnO_x nanocatalyst, and mechanisms of program-activated nanocatalyst-mediated to coordinate enhancement of tumor ablation through lysosomal damnification (stage I), GSH depletion and H_2O_2-mediated ROS generation (stage II).

based on the Fenton/Fenton-like reaction is known to be one of the recently developed cancer therapeutic strategies, however, several major factors are responsible for treating failure, such as complex intratumoral heterogeneity [8,9], inadequate catalytic efficiency of metal ions (Fe, Mn, Co) [10] and insufficient endogenous H_2O_2 [11], *etc*. Therefore, there is an desperate need for an efficient approach to enhance the production of hydroxyl radical (•OH) at the tumor site to reverse treatment failure. Recently, some plans for improving and amplifying the efficacy of H_2O_2-mediated CDT have been proposed, *e.g.*, enzyme-driven H_2O_2 supplement systems (glucose oxidase (GOx) [12] and superoxide dismutase (SOD) [13]), self-sufficiency systems (CuO_2 [14], CaO_2 [15] and BaO_2 [16] and chemotherapy drug assistance (doxorubicin (DOX) [17], platinum-related drugs [18]). These CDT-related decisions-making does not serve the effect of tumor therapy despite providing abundant H_2O_2, thus finding alternative types of treatment or combining with other treatments is a challenge at present. In addition, these external energy-triggered ROS-based tumor therapies (such as PDT or SDT) is readily limited by the finite penetration of external energy into tumor tissue and the conversion efficiency of sensitizers [19]. Anyway, much of the challenge in developing ROS-based tumor therapy is to perform unwanted internal/external stimulation at the tumor site to produce the high levels of ROS in succession for cancer treatment.

Recently, the over-developed lysosomes in tumor cells, as important sub-organelles with digestive properties, have been identified as an important target for the tumor therapy because of their special physiological environments and bio-functions [20]. Numerous studies have found that in tumor cells, lysosomes, in addition to participating in the "garbage disposal systems", also involve genetic inheritance, immunity, cell metabolism and other auxiliary functions [21]. Although in adaptable cytoprotection or rapid metabolisms plays an important position for lysosomes, this is an unfavorable signal for intelligent drug delivery system (DDS) to deliver substances (*e.g.,* drugs, proteins and small interfering RNA (siRNA)) in tumor cells because of the risk of degradation by the dynamically acidic (pH 4.5–5.5) and/or hydrolases (*e.g.*, cathepsin B) during endocytosis processes [22,23]. Therefore, the retention behavior in lysosomes is a critical barrier to effective drug delivery at the subcellular levels, and also a significant challenge. Encouragingly, once lysosomal integrity is destroyed, the possibility of inducing lysosomal membrane permeability (LMP) increases, thus accelerating cell death [24,25]. Recently, much research efforts are being devoted to the development of DDS-mediated lysosomes dissolution or lysosomal escape to enable carriage release or acidification of the cytoplasm, thereby facilitating the scaling-up of tumor therapy. Versatile DDS with unique physicochemical properties can regulate multiple lysosome-related pathways in targeted cell therapy to obtain synergistic therapeutic outcomes. Huang et al. [26] developed a therapeutic probe MP-TPEDCH based on the AIE skeleton TPEDCH and partial lysosomal target MP for fluorescence imaging to track lysosome activity and NIR radiation-activated ROS generation. Timely lysosomal escape is essential for endotrophic nano-vehicle to effectively avoid premature degradation under the acidic and hydrolytic conditions of lysosomes. Therefore, strategies with diverse functional attributes are proposed and designed to assist nanomaterials escape lysosomes, *e.g.*, the imbalance of

potential of lysosomal membrane [27], proton sponge effect-mediated lysosomal ruptures [28], and properties similar to membrane fusion by fusogenic peptides or electrostatic interactions [29]. Additionally, external trigger (Near infrared (NIR), light) induce the generation of ROS in overdeveloped lysosomes [30,31], leading to the LMP pathway by lipid peroxidation (LPO) processes, and gaining remarkable outcomes in relevant lysosomal pathway-mediated tumor therapy. Nevertheless, lysosomal LPO induced by externally mediated ROS treatment patterns are vulnerable to limited energy penetration depth and expensive equipment. As a result, recently, treatment strategies for *in situ* lysosomal activation of ROS have received increasing attention. Deng et al. prepared a series of pK_a adjustable nanoparticles in the range of 5.2–6.2, and loaded copper peroxide with H_2O_2 self-supplying, which could be used to trap copper peroxide in acidic lysosomes to produce ample catalytic ions that convert self-supplied H_2O_2 into •OH by a robust Fenton reaction after cell internalization, thereby bringing lysosome-mediated tumor therapy effectively permeated lysosomal membrane by highly reactive •OH [32]. Although lysosome-mediated tumor therapy has yielded good results, the associated reports are limited, especially in spontaneous ablation of lysosomes *in situ*.

Herein, acidity-unlocked TCPP-Cu@MnO_x ($(Mn^{II})_1(Mn^{III})_{2.1}(Mn^{IV})_{2.6}O_{9.35}$) nanocatalyst was manufactured for *in situ* unsolicited triggering of ROS generation to mediate lysosomal damage, meanwhile "nanocargo" escapes from the lysosomes to the cytoplasm to consume of intracellular glutathione (GSH) levels, as well as coordinated enhancement of ROS-related pathways, thereby leading to tumor ablation. The as-prepared TCPP-Cu@MnO_x nanocatalyst had significant stability and dispersion in normal media, in contrast, they showed TME (acid and GSH)-responsive decomposition and released their own belongings. Concurrently, TCPP-Cu@MnO_x nanocatalyst also exhibited multienzyme-like activities, such as oxidase (OXD) and peroxidase (POD). More unexpectedly, the high-yielding production of singlet oxygen ($^1O_2$) in acid condition (pH 5.0) was showed compared to neutral media (pH 7.4), with a difference of about 204 times between the two. Therefore, the integration of TCPP-Cu@MnO_x nanocatalyst reached the location of tumor cell after the blood circulation, and effectively bounded to acidic lysosomes after endocytic uptake. In this study, the entire treatment processes are divided into two stages. TCPP-Cu@MnO_x nanocatalyst with pH-switch bioreactor spontaneously produced $^1O_2$ *in situ* in acidic lysosomes, effectively inducing LMP and disrupted the integrity of the lysosomes, further causing nanocatalyst escape from lysosomes as well as partial tumor cell death (named as stage I). Meanwhile, after escaping lysosomes, TCPP-Cu@MnO_x nanocatalyst was effectively captured by high-level endogenous reducing substance of GSH, resulting in their degradation and apparent consumption of endogenous GSH. Subsequently, the Fenton-like reactions and TCPP-mediated peroxide derivatives were occurred by Mn/Cu ions and endogenous H_2O_2 in cytoplasm, followed by abundant ROS (•OH and $^1O_2$) with high cytotoxicity were obtained to further effectively induce tumor cell death (named as stage II) (Fig. 1). Thus, the strategy of programmed ROS enhancement-mediated tumor ablation have been proposed, which will provide a new window for ROS-based tumor therapy.

2. Materials and methods

2.1. Materials

Hydrogen peroxide (H_2O_2, 30 %), copper chloride hexahydrate ($CuCl_2$•$2H_2O$, 95 %), reduced glutathione (GSH, 98 %) and polyvinyl pyrrolidone K-30 (PVP, M.W. = 40,000) were bought from Shanghai Chemical Factory (Shanghai, China). Trifluoroacetic acid (CF_3COOH), tetrakis (4-carboxyphenyl) porphyrin (TCPP), 5,5-dithiobis (2-nitrobenzoic acid) (DTNB), potassium permanganate ($KMnO_4$, 98 %), 2,9-dimethyl-1,10-phenanthroline hem ihydrate (DPTH, 98 %), and 3,3',5,5'-tetramethylbenzidine (TMB) were purchased from Aladdin Reagents Company (Shanghai, China). Indocyanine green (ICG, ≥98 %) was purchased from MaoKang Biot (Shanghai, China), N,N-dimethylformamide (DMF), dimethyl sulfoxide (DMSO) and ethanol were obtained from Beijing Chemical Reagents Company (Beijing, China). Calcein acetoxymethyl ester (calcein AM), propidium iodide (PI), 2′,7′-dichlorodihydrofluorescein diacetate (DCFH-DA), and singlet oxygen sensor green (SOSG) were obtained from Sigma-Aldrich Co. (St. Louis, MO, USA). Annexin V-FITC apoptosis detection kit, cell counting kit-8 (CCK-8) and GSH/GSSG assay kit were purchased from Beyotime Biotechnology. Phosphate-buffered saline (PBS), penicillin-streptomycin (100 ×) and Dulbecco's modified Eagle's medium (DMEM) were obtained from Life Technologies Corporation (Los Angeles, CA, USA). Standard fetal bovine serum (FBS) was purchased from ExCell Bio. The ultrapure water (18.2 MU, Milli-Q, Millipore) was used throughout the experiments. All reagents and chemicals were used without further purification.

2.2. Preparation of TCPP-Cu@MnO_x nanocatalyst and ICG-labelled TCPP-Cu@MnO_x nanocatalyst

The TCPP-Cu@MnO_x nanocatalyst was prepared by modifying previous report [33]. In short, $CuCl_2$•$2H_2O$ (37.5 μmol, 6.4 mg) and TCPP (12.5 μmol, 9.9 mg) were mixed and dissolved in a mixture of DMF (15 mL) and ethanol (5 mL). After mixed solution was stirred for 15 min, PVP (5 mg) and CF_3COOH (20 μL) were added orderly, and mixed solution was heated at 80 °C. After reaction of 2 h, the final product of TCPP-Cu nanosheet was obtained by adding 20 mL water and centrifuging. Subsequently, 10 mg of TCPP-Cu nanosheet reacted with 5 mg $KMnO_4$ at room temperature for 12 h. The obtained product was purified by centrifuging and washing with water, and maintained at 4 °C.

Subsequently, indocyanine green (ICG, 1 mg) was sought as a fluorescence probe, using a simple method to load ICG on the surface of the TCPP-Cu@MnO_x nanocatalyst (1 mg/mL, 1 mL). The purified ICG-labelled nanocatalyst was collected through centrifugal (rpm = 11,000, 10 min).

2.3. Characterization

Transmission electronic microscope (TEM) images were obtained from a TEM system (JEOL JEM 2100F) with an accelerating voltage of 75 keV. Atomic force microscopic (AFM) images were taken with a Multimode-V atomic force microscope (Bruker Dimension ICON, Germany). UV–vis absorption spectra were measured on a UV-3101PC Shimadzu UV–vis spectroscope. The mean diameter of nanocatalyst was measured by the dynamic laser light scattering (ZEN 3600, Malvern Instruments). Fourier transform infrared spectroscopy (FTIR) spectra were recorded on a Nicolet 6700 FTIR spectrometer with KBr pellets in the 4000-400 cm^{-1} region. X-ray photoelectron spectroscopy (XPS) analysis was performed using an ESCALAB 250 X-ray photoelectron spectrometer with a monochromated X-ray source (Al Kα $h\nu$ = 1486.6 eV). The X-ray diffraction (XRD) patterns were used to acquire information on crystallography and measured on a PANalytical X-ray diffractometer with Cu-Kα radiation (λ = 0.15405 nm). Fluorescence spectra were obtained on a LS-55 Luminescence Spectrometer (Perkin-Elmer). Concentrations of copper and manganese were measured by inductively coupled plasma (ICP, ThermoScientific Xseries II, USA). The relevant ROS were measured by electron spin resonance (ESR, JES-FA 200).

2.4. Ion release

TCPP-Cu@MnO_x nanocatalyst (2 mg/mL, 0.5 mL) was immersed in different media (pH 7.4 and pH = 5.0 + 10 mM GSH, simulating normal media and tumor microenvironment, respectively). The supernatant was collected at pro-expected times by centrifugal method (rpm = 13,000, 15 min), and detected *via* the inductively coupled plasma (ICP) technology.

2.5. Acid-responsive $^1O_2$ generation

Briefly, 20 μL of TCPP-Cu@MnO_x nanocatalyst (1 mg/mL) and 15 μL of singlet oxygen sensor green (SOSG) (1 mM dissolved in DMSO) were reacted under different pH values (7.4, 6.5, 6.0 and 5.0), and keeping the total volume of 1 mL. The reacted solution was measured by fluorescence spectroscopy. In addition, we also evaluated fluorescence changes in normoxia or hypoxia (N_2 gas) conditions.

2.6. Multienzyme activities estimation

The POD-like activity of TCPP-Cu@MnO_x nanocatalyst was measured through using 3,3',5,5'-tetramethylbenzidine (TMB) as a probe. Simply, TMB oxidation experiment was performed by mixing TMB (16 mM, 50 μL), H_2O_2 (5 mM) and TCPP-Cu@MnO_x nanocatalyst (1 mg/mL, 10 μL) in PBS (940 μL) with different pH values (pH 7.4, 7.0, 6.5, 6.0 and 5.0). After 20 min of reaction, the supernatant was characterized by UV–vis spectroscopy at wavelength range of 550–750 nm. Moreover, we also assessed in the introduction of different concentrations of H_2O_2 (0, 0.5, 1, 2, 4, 6, 8, and 10 mM) by UV–vis spectroscopy. Additionally, the mix systems were also tested in hypoxia and normoxia condition at different time points. The whole experimental system was kept at 1 mL.

The OXD-like activity of TCPP-Cu@MnO_x nanocatalyst was assessed using TMB probe. Simply, different concentrations of TCPP-Cu@MnO_x nanocatalyst (0, 5, 10, 15, 20, 25 and 35 μg mL^{-1}) reacted with TMB (50 μL, 16 mM) at pH 5.0 PBS for 20 min, and was then measured by UV–vis spectroscopy. Additionally, we also assessed the reaction changes of TMB solution (16 mM, 50 μL) containing TCPP-Cu@MnO_x nanocatalyst (1 mg/mL, 10 μL) at different pH values (7.4, 7.0, 6.5, 6.0 and 5.0). Moreover, PBS solution (pH 5.0) including either TCPP-Cu nanosheet (10 μL, 1 mg/mL) + $MnCl_2$ (0.5 mM) or TCPP-Cu nanosheet (10 μL, 1 mg/mL) were used as control measurements, respectively.

2.7. Detection of ROS by ESR technology

5,5-dimethyl-1-pyrroline N-oxide (DMPO) and 2,2,6,6-tetramethyl-1-piperinedinyloxy (TEMP), as capturing agents, were employed as probe to detect •OH and $^1O_2$ respectively. Briefly, TCPP-Cu@MnO_x nanocatalyst (10 μL, 2 mg/mL) was dispersed into PBS solution (pH 5.5 and pH 7.4), and then added TEMP (20 μL) to assess $^1O_2$ generation. Moreover, TCPP-Cu@MnO_x nanocatalyst (10 μL, 2 mg/mL) was added into PBS (pH 5.0) with and without GSH (100 μL, 0.67 mM). Then, H_2O_2 solution (10 μL, 1 M) were added, and kept final solution was 1 mL. After 30 min of treatment, DMPO (10 μL) was added and detected by ESR technology.

2.8. GSH consumption and Cu ion detection

TCPP-Cu@MnO_x nanocatalyst was con-incubated in PBS (pH 7.4) with different concentrations of GSH (0, 0.625, 1.25, 2.5, 5, and 10 mM). After 20 min of reaction, 1 mL mixture was transferred and added into 2 mM 5,5-dithiobis (2-nitrobenzoic acid) (DTNB) ethanol solution. After shaking, the absorbance changes were observed by UV–vis spectrophotometer.

To investigate the valence of copper ions in TCPP-Cu@MnO_x nanocatalyst, we used a copper ion probe, 2,9-dimethyl-1,10-phenanthroline hem ihydrate (DPTH), through UV–vis spectroscopy. In short, TCPP-Cu@MnO_x nanocatalyst and DPTH probe [34] were con-incubated in PBS (pH 5.0) for 8 h. Subsequently, the supernatant was collected through the centrifugal (rpm = 13000, 10 min). meanwhile, the additive reductant GSH (5 mM) continued to react to 3 min. Finally, the reacted solution was detected by UV–vis spectrophotometer. Additionally, other controlled solution groups (pH 5.0 PBS), including Cu^{2+} + DPTH, Cu^{2+} + DPTH + GSH, TCPP-Cu@MnO_x + DPTH + GSH, also were detected.

2.9. Detection of ROS after GSH processing

The Cu^+/Mn^{2+}-mediated Fenton-like reaction-generated •OH was analyzed by UV–vis spectroscopy. Briefly, TCPP-Cu@MnO_x nanocatalyst (1 mg/mL, 20 μL) and methylene blue (MB, 10 μg/mL, 20 μL) were co-cultured with PBS (pH 5.0) containing the different contents of GSH (0, 0.625, 1.25, 2.5 and 5.0 mM). Then, the reacted solution was induced to produce •OH by culturing in 5 % CO_2, 25 mM $NaHCO_3$ buffer solution and 10 mM H_2O_2 solution for 30 min and was monitored by UV–vis method. Additionally, their reaction process was unchanged and only replaced reactants, such as reaction buffer: 25 mM $NaHCO_3$/5 % CO_2, [Mn] = 0.5 mM, [H_2O_2] = 10 mM, [Cu] = 1 mM, and [GSH] = 5 mM.

The GSH/H^+-treated TCPP-Cu@MnO_x nanocatalyst-mediated $^1O_2$ generation was tested by SOSG probe. In short, the process of GSH/H^+-treated TCPP-Cu@MnO_x nanocatalyst yet unchanged, then reaction solution was added to SOSG probe (15 μL, 1 mM) containing H_2O_2 (10 mM), and continuously reacted 20 min. Finally, the mix solution was tested by fluorescence spectrum.

2.10. Cell culture

4T1 cells (mouse breast cancer cells), IEC-6 cells (rat small intestine crypt epithelial cell lines) and CT26 cells (mouse colon cell lines) were cultured in fresh Dulbecco's Modified Eagle's Medium (DMEM, containing 10 % inactivated fetal bovine serum (FBS), 1 % penicillin and streptomycin). All cells were cultured under a humidified atmosphere with 5 % CO_2 and 95 % air at 37 °C. All cells were obtained from Cell Resource Center, IBMS, CAMS/PuMC (Beijing, China).

2.11. Lysosomes damnification

The damnification of lysosomes were assessed by intracellular fluorescence staining. 4T1 cells were seeded into 6-well plates at a density of 0.8×10^5 cells per well. And then these cells were treated with different TCPP-Cu@MnO_x nanocatalyst concentrations (10 and 50 μg mL^{-1}). Subsequently, the endo/lysosomes after 8 h of treatment were labelled through the utilization of LysoTracker@green probe, and the specific manipulation was based on the manufacturer's instructions. Finally, these cells were stained with DAPI for 10 min and observed through laser scanning confocal microscopy (CLSM).

In addition, in view of above operations, the changes of lysosomes with different treatment times (0, 4 and 8 h) were also assessed by flow cytometry. Simultaneously, the cell survival rates with different times were also detected.

2.12. Detecting ROS by DCFH-DA in vitro

4T1 cells were cultured on a 6-well plate and then treated with different concentrations TCPP-Cu@MnO_x nanocatalyst (10 and 50 μg/mL). Subsequently, after 24 h of cultivation, the medium was replaced with a fresh cell culture medium, and the DCFH-DA (10 μg/mL) probe continued to incubate for 30 min. Finally, the cells were observed by CLSM method.

Additionally, to understand the type of ROS produced by TCPP-Cu@MnO_x nanocatalyst processing cells, we evaluated by adding different quenching agents. In practice, 4T1 cells were seeded into five culture dishes (2×10^5 cells per dish). Then, 4T1 cells were incubated with 1 mL of DMEM containing TCPP-Cu@MnO_x nanocatalyst (50 μg/mL). After 12 h, each dish was washed with PBS and added with of corresponding ROS quenchers (NaN_3, isopropanol and benzoquinone) at the concentration of 1 mM, respectively. After 10 min, the treated cells were washed again with PBS, and the DCFH-DA (10 μg/mL, 1 mL) probe was added into each well. The fluorescence results were captured by flow cytometry after 30 min of incubation.

Moreover, the different pH culture media-treated 4T1 cells were also investigated to generate ROS levels. In short, the different pH culture

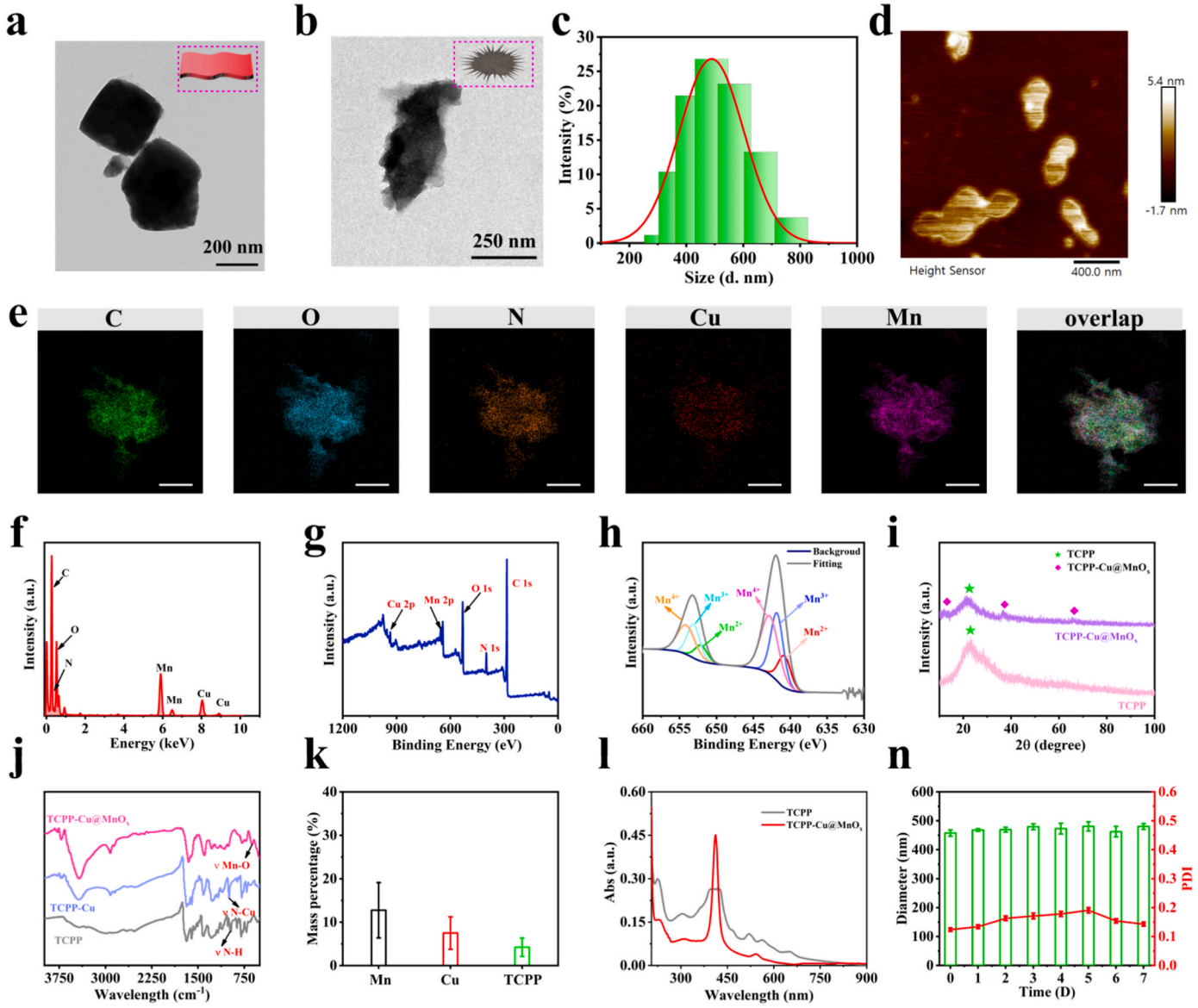

Fig. 2. Composition and structure characterization of TCPP-Cu@MnO_x nanocatalyst. (a, b) TEM images of TCPP-Cu nanosheet and TCPP-Cu@MnO_x nanocatalyst. (c, d) Particle size distributions and AFM image of TCPP-Cu@MnO_x nanocatalyst. (e) The element mappings of TCPP-Cu@MnO_x nanocatalyst, including C, O, N, Cu and Mn. (f) EDS analysis of TCPP-Cu@MnO_x nanocatalyst. (g) XPS spectrum of TCPP-Cu@MnO_x nanocatalyst. (h) XPS spectrum of wide-scan, Mn 2p of TCPP-Cu@MnO_x nanocatalyst. (i) Powder X-ray diffraction (XRD) of TCPP and TCPP-Cu@MnO_x nanocatalyst. (j) The FT-IR of TCPP, TCPP-Cu and TCPP-Cu@MnO_x nanocatalyst. (k) The ingredient content of Mn, Cu and TCPP in TCPP-Cu@MnO_x nanocatalyst. (l) The UV–vis absorption spectra of TCPP and TCPP-Cu@MnO_x nanocatalyst. (m) Particle sizes and PDI values of TCPP-Cu@MnO_x nanocatalyst at different times.

media (pH 7.4 and pH 6.5) containing TCPP-Cu@MnO_x nanocatalyst (10 μg/mL) were used to cultivate 4T1 cells. After 12 h of treatment, the DCFH-DA (10 μg/mL) probe was added and detected using flow cytometry.

2.13. Lysosomal lipid peroxidation (LPO) detection

4T1 cells plated on confocal dishes were exposed to the different concentrations of TCPP-Cu@MnO_x nanocatalyst (10 and 50 μg/mL) for 8 h. After washing twice with PBS, the cells were stained with C11-$BODIPY^{581/591}$ dye (10 μM) for 30 min, and then observed with CLSM.

2.14. Cytotoxicity assay

4T1 cells, IEC-6 cells and CT26 cells were cultured in standard cell media at 37 °C in a 5 % CO_2 atmosphere. For example, 3×10^5 4T1 cells were seeded into 96 well plates, and then TCPP-Cu@MnO_x nanocatalyst was added into in different concentrations (0, 0.625, 12.5, 25, 50 μg mL^{-1}). After 24 h, relative cell viability was determined by cell counting kit-8 (CCK-8) assay.

2.15. Live/dead and apoptosis assay

4T1 cells were seeded onto a glass-covered 6-well plate to allow attachment, and then TCPP-Cu@MnO_x nanocatalyst (10 and 50 μg mL^{-1}) was added for 24 h. Subsequently, these media were removed and washed twice with PBS. A mixed staining solution of propidium iodide (PI, 8 μM) and Calcein acetoxymethyl ester (Calcein AM, 2 μM) was freshly prepared and incubated with cells for 30 min. Finally, these cells were washed with PBS and immediately observed by CLSM.

4T1 cells were seeded into 6-well culture plates at a density of 3×10^5 cells per well and treated with PBS or TCPP-Cu@MnO_x nanocatalyst

(10, 25 and 50 μg mL^{-1}) at 37 °C for 24 h, respectively. Lastly, the obtained single cell suspension was stained with Annexin V-FITC apoptosis detection kit for flow cytometry.

2.16. Detection of intracellular GSH changes

4T1 cells (3×10^5 per well) were inoculated into 6-well plates and cultured at 37 °C, 5 % CO_2, and treated with PBS and TCPP-Cu@MnO_x nanocatalyst (10, 25, 50 μg mL^{-1}) for 12 h, respectively. The amount of GSH was analyzed by GSSG/GSH assay kits according to the manufacturer's protocol.

2.17. Animals

All animal experiments were approved by the institutional ethics committee of Shanghai Chest Hospital and all procedures were performed according to the rules of the Institutional Animal Care and Use Committee of Shanghai Chest Hospital (Approval Number: KS22004). All BALB/c mice were provided by Sibeifu Biotechnology Co., Ltd (Beijing, China).

2.18. Biocompatibility evaluation in vivo

To assess the cytotoxicity and biosafety of TCPP-Cu@MnO_x nanocatalyst in vivo, health BALB/c mice were randomly divided into two groups (n = 6). After adaptive feeding for one week, TCPP-Cu@MnO_x nanocatalyst (100 μL, 1 mg/mL) was intravenously administered into mice. The body weight of mice were recorded per two days during next 20 days. Notablely, in fifth and fifteenth days respectively, two mice were removed from each group, and blood samples of mice were collected by extracting eyeball for further blood biochemistry and blood routine analysis (including aspartate aminotransferase (AST), alanine aminotransferase (ALT), blood urea nitrogen (BUN), and creatinine (CREA), and so on.), as well as main organs (heart, liver, spleen, lung and kidney) were stained by H&E.

2.19. Bioluminescence imaging in vivo

4T1 tumor-bearing mice were established and were administered with 100 μL ICG-marked TCPP-Cu@MnO_x nanocatalyst solution *via* caudal vein. Fluorescence signals at tumor sites were monitored at 2 h, 4 h, 12 h, and 24 h after injections on the Fluorescence Imaging System for Small Animals (VISQE In vivo Smart-LF, South Korea). After 24 h post-injections of TCPP-Cu@MnO_x nanocatalyst, the mice were sacrificed, and the tumor and other organs (heart, liver, kidney, spleen and lung) were obtained. Subsequently, *ex vivo* fluorescence imaging and photographing were implemented.

2.20. Anti-tumor effect in vivo

4T1 tumor cells (cell count 5×10^5) were inoculated subcutaneously on BALB/c mice (6–8 weeks old). After 7 days of feeding, tumor volume reached approximately 70–80 mm^3 (tumor volume = (tumor length) × (tumor width)^2/2). Then, tumor-bearing mice were randomly divided into three groups (n = 5): (a) control group (PBS, 100 μL), (b) TCPP-Cu@MnO_x groups (2.5 mg/kg and 5 mg/kg, 100 μL). All mice were administered at prescribed every 2 days for 4 days by intravenous (*i.v.*) injection. During treatment, the weight and volume of mice were recorded and calculated. On the 27th day, all mice were executed and tumors were removed and weighed. At the same time, all mice's orbital blood were collected for blood testing. Tumor sections of each group were further studied by hematoxylin and eosin (H&E), terminal deoxynucleotidyl transferase mediated dUTP nick end labeling (TUNEL) staining assay and Ki-67 staining.

2.21. Statistical analysis

Data were presented as mean ± standard deviation (SD) through at least three experiments. Statistical analysis was performed using Student's *t*-test for two-group differences. A p-value <0.05 was considered statistically significant: ns: no significant, *p < 0.05,**p < 0.01, and ***p < 0.001.

3. Results and discussion

3.1. Preparation and characterization of TCPP-Cu@MnO_x nanocatalyst

The procedure for synthesizing TCPP-Cu@MnO_x nanocatalyst, briefly, was involved to two stages, as shown in Fig. 1. Firstly, TCPP-Cu nanosheet with a uniform and suitable nano-scale metal-organic framework (MOF) was prepared according to previously reported literature [33]. The as-prepared TCPP-Cu nanosheet was red powder by freeze drying, and displayed a rectangular-like morphology, in which about 254 nm in length and 265 nm in width, though transmission electron microscopy (TEM) testing (Fig. 2a and S1a, Supporting **information**). The consequences of dynamic light scattering (DLS) revealed their narrow size distribution and appropriate nanoparticle size, where polydispersity index (PDI) value was 0.136 and average size was 267 nm (Fig. S1a), due to hydrophilic PVP surface modification. The negatively charged TCPP-Cu nanosheet was −31 mV (Fig. S1b) because of rich carboxyl group of TCPP ligand exposure during coordination processes. In addition, as shown in Fig. 2j, the emergence of a new peak of 996 cm^{-1}attributed to N-Cu stretching of TCPP-Cu was exhibited by comparing with TCPP, further suggesting that copper ion was also coordinated in the porphyrin center of TCPP in addition to coordination node [35].

To endow nanomaterials biocatalytic properties, subsequently, though using potassium permanganate ($KMnO_4$) surface redox modification, MnO_x-decorated TCPP-Cu was obtained, and named as TCPP-Cu@MnO_x nanocatalyst (Fig. 1). TEM imaging showed the shape of TCPP-Cu nanosheet surface forming similar pleated burr morphology (Fig. 2b), and particle size was converted to 470 nm and PDI was 0.21 (Fig. 2c) by DLS measurement. Moreover, TCPP-Cu@MnO_x nanocatalyst had a thickness of averagely 3.3 nm by atomic force microscopy (AFM) (Fig. 2d and S3). Moreover, the characteristic infrared peak of MnO_x component at 628 cm^{-1} was presented compared with TCPP-Cu nanosheet, demonstrating the successful grooming (Fig. 2j). In addition, changes that occurred redox reaction in components on TCPP-Cu nanosheet surface caused fluctuations in surface potential, which was −40.2 mV (Fig. S2a). To study the elemental distribution of TCPP-Cu@MnO_x nanocatalyst, the surface homogeneous distribution of C, N, O, Cu and Mn were displayed in elemental mapping images (Fig. 2e). Moreover, the X-ray energy dispersive spectroscopy (EDS) and the full-range survey of XPS spectrum of TCPP-Cu@MnO_x nanocatalyst showed the coexistence of Mn element (Fig. 2f and g), further demonstrating the successful construction of MnO_x modification, consistent with element mappings results. In view of the importance of metal valence state in the course of catalytic process as well as the study of the x value of TCPP-Cu@MnO_x nanocatalyst, the high resolution spectrum of Mn element was analyzed (Fig. 2h). The binding energy of Mn 2p was split into three pairs of characteristic peaks, which corresponds to Mn^{4+}, Mn^{3+}, and Mn^{2+} [36], and these Mn $2p_{3/2}$ results showed that trivalent and quadrupvalent Mn were dominant valence states, with relative content of about 37.4 % and 45.0 %, whereas bivalent manganese was less distributed and accounted for only about 17.6 %, suggesting that TCPP-Cu@MnO_x nanocatalyst have a high activity to generate ROS and GSH consumption capacity. Thus, the chemical formula of MnO_x component was proposed as $(Mn^{II})_1(Mn^{III})_{2.1}(Mn^{IV})_{2.6}O_{9.35}$. To see the crystallographic structure of TCPP-Cu@MnO_x nanocatalyst, X-ray diffraction (XRD) was employed and proved obtained materials were birnessite-type MnO_2 with MnO_x surfaces by typical peaks (2θ) at 36.49°

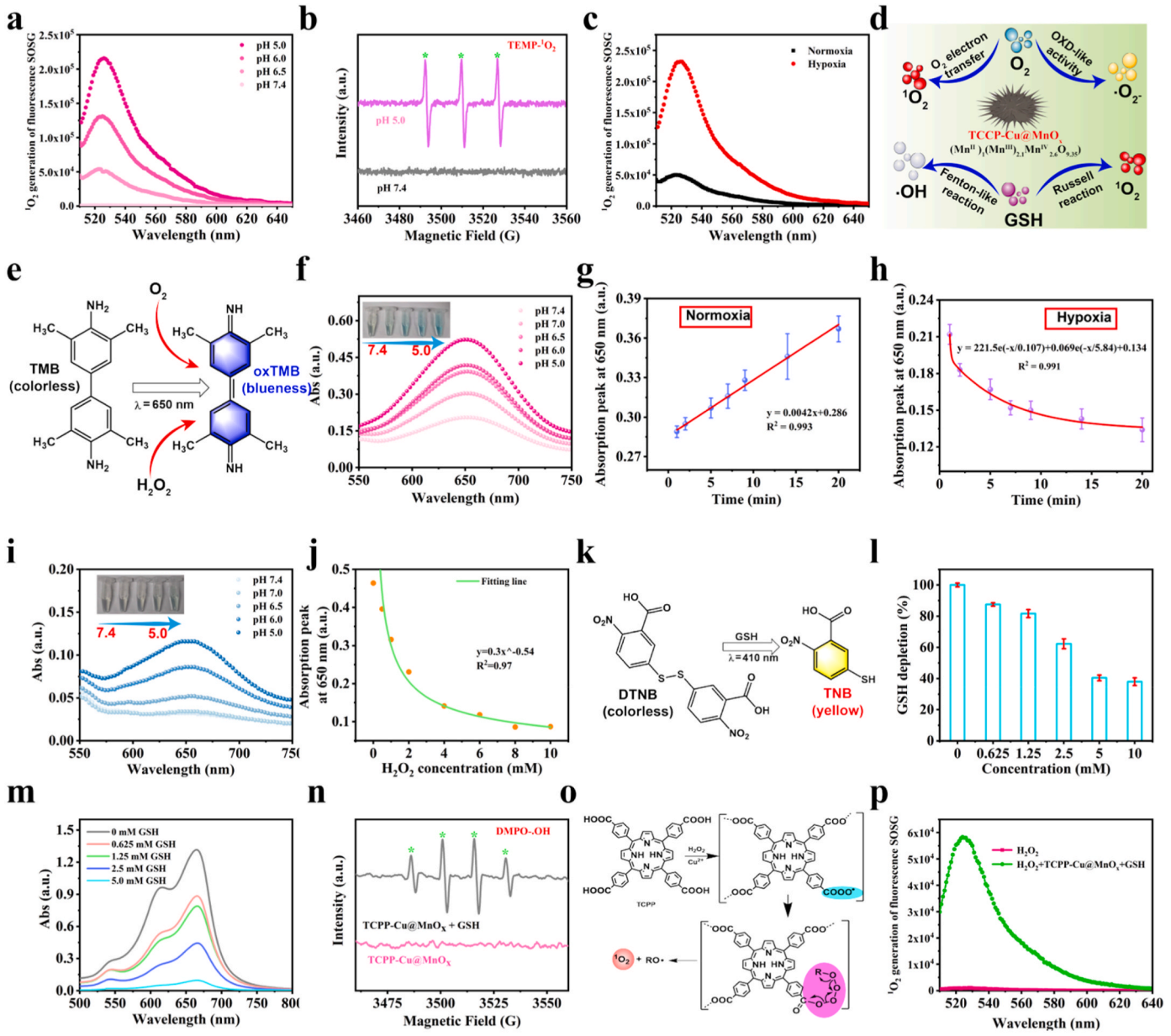

Fig. 3. ROS generation capabilities and GSH consumption. (a) The $^1O_2$-generating capability in diverse pH media (pH = 7.4, 6.5 6.0 and 5.0) was measured by SOSG fluorescence probe. (b) ESR spectra of $^1O_2$ generation in different media (pH = 7.4 and 5.0). (c) The changes of $^1O_2$ generation were detected by SOSG fluorescence at normoxia and hypoxia condition. (d) Schematic illustration of the multifunctional process of TCPP-Cu@MnO_x nanocatalyst. (e) The corresponding equation of TMB in TCPP-Cu@MnO_x nanocatalyst treatment. (f) pH-dependent UV–vis absorption spectra for TMB-processed TCPP-Cu@MnO_x nanocatalyst, *inset*: photographs of these reaction changes. (g, h) The fitting curve of time correlation at 652 nm peak in normoxia (g) and hypoxia (h) conditions. (i) UV–vis spectra of oxTMB containing TCPP-Cu@MnO_x nanocatalyst and H_2O_2 with different pH values (7.4, 7.0, 6.5, 6.0 and 5.0), inset: photograph of these reaction changes. (j) The fitting curve of H_2O_2 concentration correlation at 652 nm peak. (k) Determination of the chemical reaction formula of GSH by DTNB method. (l) Changes in GSH depletion in the different doses of GSH solution treated with TCPP-Cu@MnO_x nanocatalyst. (m) The UV–vis absorption curves of MB solution containing GSH (0–5 mM), TCPP-Cu@MnO_x nanocatalyst (1 mg/mL) and H_2O_2 (10 mM), under $NaHCO_3/CO_2$ conditions. (n) ESR spectra analyses of •OH levels in reaction mixtures added with DMPO as signal trap. (o) The mechanism of TCPP-relevant product-induced Russell reaction. (p) The H_2O_2-medaited $^1O_2$ generating by SOSG fluorescence testing after GSH-treated TCPP-Cu@MnO_x nanocatalyst.

and 65.81° respectively (Fig. 2i), and the remaining emergence of peaks were caused by the tetragonal structure of two dimensional (2D) TCPP-Cu [33,37]. Furthermore, to investigate the valence of copper ions in TCPP-Cu@MnO_x nanocatalyst, we used a copper ion probe, 2, 9-dimethyl-1,10-phenanthroline hem ihydrate (DPTH), through UV–vis spectroscopy. The study found that TCPP-Cu@MnO_x nanocatalyst can be effectively destroyed under acidic condition (Fig. S6b), thus significantly releasing metal ions. Thus, after cultivating 12 h in pH 5.0 PBS, the supernatant did not change when the probe was added, compared to GSH-treated Cu^{2+} soultion. Excitingly, when the reductant GSH was added, the collected colorless supernatant was converted to yellow color, mainly due to the reduction of Cu^{2+} ions to Cu^+ (Fig. S2b). In conclusion, it is shown that the main valence form of copper in TCPP-Cu@MnO_x nanocatalyst was bivalent.

From the observation of UV–vis absorption spectra in Fig. 2l, the appearance of a strong absorption peak at 412 nm was observed in TCPP-Cu@MnO_x nanocatalyst, indicating the redox reaction produces MnO_x analogues [36]. Meanwhile, the characteristic peak of Q band of

TCPP monomer was replaced by a peak at 541 nm, illustrating the successful synthesis of MnO_x-coated TCPP-Cu [33]. Moreover, the component of TCPP-Cu@MnO_x nanocatalyst was analyzed, and testing results showed that the mass percentages of Mn and Cu in nanocatalyst were 12.2 % and 8.1 %, respectively, by inductively couple plasma (ICP-OES) measurement (Fig. 2k). The TCPP content in TCPP-Cu@MnO_x nanocatalyst was computed by UV–vis absorption fitting curve of TCPP, and the calculated value was 4.2 % (Fig. S4).

3.2. Stability assessment and degradation behavior

The long-term stability and homo-disperse of nanoparticles are essential in medium, especially in nanoparticles-mediated tumor therapy [36]. Thus, the time-dependent stability of TCPP-Cu@MnO_x nanocatalyst was detected by UV–vis technology and DLS method. These relevant testing results showed no significant fluctuations over cultured time through including hydrodynamic size and PDI (Fig. 2n), as well as UV–vis spectra (Fig. S5c), demonstrating the stability and no shedding of TCPP-Cu@MnO_x nanocatalyst in water. Thereafter, the resistance to instability of TCPP-Cu@MnO_x nanocatalyst has been explored in diverse media (PBS (pH 7.4) and 10 % fetal calf serum (FBS)). After 7 days of cultivation, the changes of these hydrodynamic size were minimal, which demonstrated that TCPP-Cu@MnO_x nanocatalyst had a well-defined distribution and no significant aggregation occurred over time (Figs. S5a and S5b), and thus clarifying that its have potential biological application value. It is well known that tumor cells form unique tumor microenvironments (TME), such as acidic environment and high level of GSH, due to special growth and proliferation pathways compared to normal tissue [38,39]. Based on this, the degradation behaviors of TCPP-Cu@MnO_x nanocatalyst at diverse pH values, GSH concentrations (Fig. S6a), or H_2O_2 levels (Fig. S7) were estimated. As shown in Fig. S6b, the characteristic UV–vis absorption peak at 412 nm gradually weakened as the acidity increases from 7.4 to 5.0. Similarly, the downward trend of absorption peak at 412 nm accelerated when additional reduce substance of GSH was added (Fig. S6c). As a result, the intensity of absorption peak (412 nm) of these associated properties decreased as GSH and/or acid trigger degradation of the MnO_x layer of nanocatalyst (Fig. S6d), and these outcomes are consistent with similar MnO_x derivatives [40,41]. Additionally, TCPP-Cu@MnO_x nanocatalyst was also effectively degraded when additional hydrogen peroxide was introduced (Fig. S7). Subsequently, after 24 h of incubation, in pH 5.0 + 10 mM GSH condition (simulating the tumor microenvironment), the brown flocculent precipitates appeared at the bottom of bottle and the supernatant was transparent (Fig. S6e), indicating that TCPP-Cu@MnO_x nanocatalyst completely degraded and fall off insoluble TCPP associated substances. Furthermore, the changes of hydrodynamic size of nanocatalyst occurred as 10 mM GSH + pH 5.0 PBS culture time increase though DLS tracing (Fig. S8), and its size undergone a time-driven process of change from small to large, further elucidating that nanocatalyst had the capability of degradation under acid/GSH. Anyway, these results of pH 7.4 medium treated material stability and acid/GSH triggered degradation behavior will provide a guarantee for TCPP-Cu@MnO_x nanocatalyst in blood-circulation, as well as TME-responsive degradation pathway lay foundation for subsequent enhanced tumor treatment.

3.3. ROS generation, multienzyme activities estimation and GSH depletion in vitro

Currently, including insufficient external excitation depth, narrow treatment area, *etc.*, these irresistible intrinsic factors have limited development of emerging exterior (*e.g.*, ultrasound, light and electromagnetism)-stimulated $^1O_2$ generation patterns [42]. Therefore, we first discovered that TCPP-Cu@MnO_x ($(Mn^{II})_1(Mn^{III})_{2.1}(Mn^{IV})_{2.6}O_{9.35}$) nanocatalyst have acid-triggered the generation of $^1O_2$ capacity in mild acid solutions (Fig. 3d). To explore $^1O_2$ situation, the SOSG (singlet oxygen sensor green, a ROS probe) was employed to detect $^1O_2$ production. As shown in Fig. 3a, TCPP-Cu@MnO_x nanocatalyst was treated by SOSG with different pH values (7.4, 6.5, 6.0 and 5.0) and then detected by fluorescence spectrum. It was proved that the fluorescence intensity of SOSG was related to acidity and showed the fluorescence enhancement trend with acidity enhancement, indicating that acidity activated $^1O_2$ production. Notably, the SOSG fluorescence intensity was about 204 times stronger in pH 5.0 than that pH 7.4 cultivation (Fig. S10a), and extending the culture time to 24 h, the fluorescence intensity of SOSG continued to increase, enhancing about 8.5 times compared to the original fluorescence intensity (Fig. S10b). Moreover, by comparing normoxia-treated group, the fluorescence intensity of SOSG in hypoxia-cultured group obviously diminished (Fig. 3c), indicating that oxygen involved the production of $^1O_2$. The electron spin resonance (ESR) detection was also performed to verify pH-responsive $^1O_2$ generation. Undergoing pH 5.0 with 2,2,6,6-tetramethyl-4-piperidone (TEMP, single-line oxygen capture agent) incubation, we found that a typical peak signal of 1:1:1 was produced, indicating the generation of $^1O_2$, whereas in 7.4 media there was no significant $^1O_2$ generation in similar experimental operations (Fig. 3b). Theoretically, the acid-induced $^1O_2$ generation is mainly due to the abundance of Mn (III) in TCPP-Cu@MnO_x nanocatalyst, *i.e.*, Mn (III)-driven related catalytic activity to generate $^1O_2$ [41,43] by the O_2 electron transfer effect (Fig. S9), thus providing an opportunity for the induction of lysosomal membrane permeability (LMP) in acidic lysosomes.

Given the properties of enzyme-like activation of the MnO_x component, we also evaluated the catalytic properties of TCPP-Cu@MnO_x nanocatalyst (Fig. 3e). No blue color appeared at the wavelength of 550–750 nm for free 3,3',5,5'-tetramethylbenzidine (TMB). Conversely, the TMB solution containing TCPP-Cu@MnO_x nanocatalyst produced a strong characteristic absorption peak at 652 nm, with the color converted from colorless to blue. As pH value decreasing, the absorption peak also increased and showed an pH-dependent growth tendency (Fig. 3f), further revealing that the acid promoted TMB oxidation (named as oxTMB). Additionally, time- and dose-dependent behaviors of oxTMB generation were displayed and each other was a linear correlation (Fig. 3g and S12). Amazingly, hypoxia inhibited TMB oxidation compared to normal oxygen environment and showed a nonlinear reduction (Fig. 3h). In summary, TCPP-Cu@MnO_x nanocatalyst had oxidase-like activity and was susceptible to oxygen and pH interference. Additionally, the oxTMB no appeared in free TCPP-Cu nanosheet and TCPP-Cu nanosheet $+Mn^{2+}$ mix solution (Fig. S11). Theoretically, oxidase-like activity occurs mainly because MnO_x-coated TCPP-Cu induces the conversion of O_2 to $O_2^{\bullet-}$ through electron transfer [43]. Meanwhile, this result plays an important role in the production of acid-activated $^1O_2$, namely, the conversion pathway of O_2-$O_2^{\bullet-}$-$^1O_2$ to provide a powerful guarantee (Fig. S9).

As shown in Fig. 3i, the oxTMB weakened significantly in the extra presence of H_2O_2 (10 mM), meanwhile, they also showed a enhancement to acidity. In addition, the process of TMB oxidation was susceptible to strong interference with H_2O_2 concentration factor and showed exponential reduction (Fig. 3j and S13). In conclusion, TCPP-Cu@MnO_x nanocatalyst exhibited poor POD-like enzyme catalytic properties, maybe due to H_2O_2 involvement in the destruction of structure integrity and participation in chemical reactions.

It is known that the high-valence metal ions (Mn (III, IV) and Cu (II)) are easily converted to reduced status in the presence of reducing agents such as GSH [44]. As expected, the high activity of TCPP-Cu@MnO_x nanocatalyst could significantly be consumed *via* reducing agent GSH, thereby prompting the disintegration of nanocatalyst, and releasing low-valence status ions and TCPP-associated products. In view of the high expression of H_2O_2 [33] and GSH [38,39] in tumor cellular, we further assessed GSH depletion and H_2O_2-mediated ROS generation *in vitro*. Due to the presence of high-valence copper and manganese ions, the GSH depletion ability of TCPP-Cu@MnO_x nanocatalyst was assessed using 5,5-dithiobis(2-nitrobenzoic acid) (DTNB, a GSH indicator)

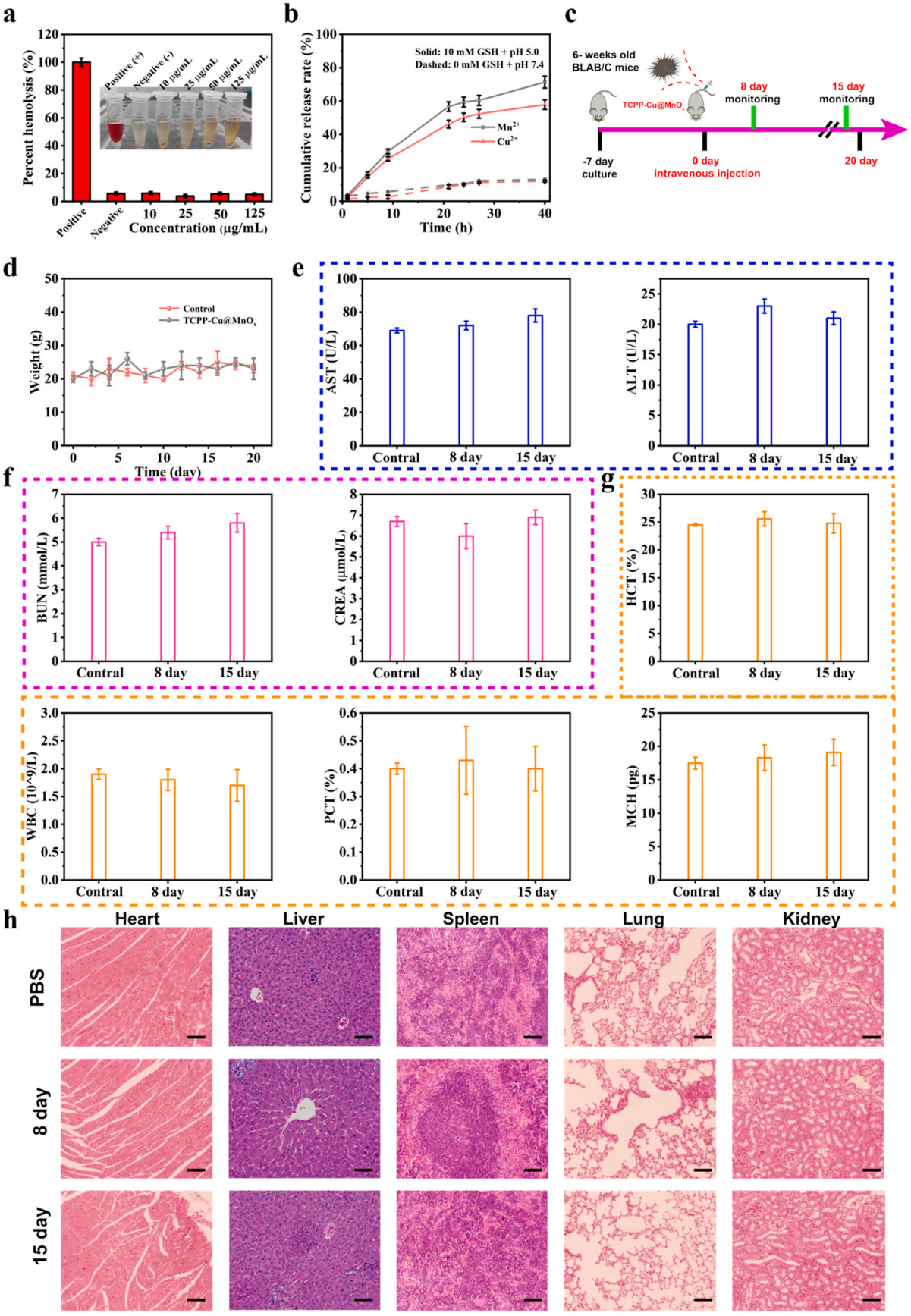

(caption on next page)

Fig. 4. (a) Hemolytic activity of TCPP-Cu@MnO_x nanocatalyst, insert: photograph of hemolytic activity of TCPP-Cu@MnO_x nanocatalyst. (b) The released percentage of Mn and Cu over time with different conditions by ICP. (c) Chematic diagram of TCPP-Cu@MnO_x nanocatalyst treatment of health BALB/c mice. (d) Body weight changes of BALB/c mice after injection of PBS or TCPP-Cu@MnO_x nanocatalyst (100 μL). (e) Blood levels of aspartate aminotransferase (AST) and alanine aminotransferase (ALT) as liver function markers. (f) Blood urea nitrogen (BUN) and creatinine (CREA) represent as kidney function markers. (g) Blood routine analyses and blood chemical indexes of mice in different treatment groups at the end of the therapeutic evaluation. The complete blood data: hematocrit (HCT), white blood cell (WBC), procalcitonin (PCT) and mean corpuscular hemoglobin (MCH). (h). Representative H&E stained major organ tissue sections of groups, scale bar: 100 μm. Data represent mean ± standard deviation.

measurement (Fig. 3k). After adding DTNB into different doses GSH-treated TCPP-Cu@MnO_x nanocatalyst, the characteristic absorbance peak at 412 nm diminished (Fig. 3l), indicating that nanocatalyst had significant GSH consumption capacity. Thus, TCPP-Cu@MnO_x nanocatalyst-mediated consumption reaction of GSH will help to enhance cell oxidation damage and amplify ROS-based therapeutic effect. Methylene blue (MB, free radical indicator) solution containing H_2O_2 (10 mM) and different concentrations GSH-treated TCPP-Cu@MnO_x nanocatalyst (1 mg/mL) co-incubated for 20 min in 5 % CO_2, 25 mM $NaHCO_3$ buffer solution, followed by UV–vis testing. The absorbance peak at 665 nm decreased as concentration of GSH increasing (Fig. 3m), which displayed a analogous GSH-responsive MB degradation behaviors, suggesting that GSH regulated Cu/Mn ions release to enhance H_2O_2-mediated the production of •OH with high cytotoxicity (Fig. S14). Additionally, GSH-treated TCPP-Cu@MnO_x nanocatalyst solution containing H_2O_2 (10 mM) could be produce •OH through ESR detection, while in pH 7.4 without GSH solution, there was no characteristic signal peak (1:2:2:1 quartet signal) of •OH (Fig. 3n). Therefore, GSH could effectively degrade TCPP-Cu@MnO_x nanocatalyst and released Mn^{2+} and Cu^{+} ions, in turn, release ions involved in the Fenton-like reaction to produce •OH in the presence of H_2O_2. In addition, GSH also triggered the release of TCPP-associated nano-debris from TCPP-Cu@MnO_x nanocatalyst. Interestingly, research findings that TCPP-associated nano-debris could induce the production of $^1O_2$ in mild H_2O_2 by the Russell reaction through SOSG fluorescence detection (Fig. 3o and p and S15) [33,44].

3.4. Biosafety evaluation and fluorescence in vivo

The biosafety and effectiveness of TCPP-Cu@MnO_x nanocatalyst as a fresh synthetic material cannot be ignored in the biological field. Therefore, the hemolysis results displayed that the percentages of hemolysis in all samples was less than 5.6 % after culture at different concentrations, even the concentration of nanocatalyst reached 150 μg/mL, indicating a relatively high biosafety of injection administration (Fig. 4a).

Subsequently, we also evaluated the release behavior of ions (Mn ion and Cu ion) from TCPP-Cu@MnO_x nanocatalyst. The accumulate release profiles of Cu ion or Mn ion showed time-dependence sustained-release properties (Fig. 4b). The Mn ion release rate from TCPP-Cu@MnO_x nanocatalyst under tumor conditions (pH 5.0 and 10 mM GSH) was up to 70.3 % within 40 h, while the release rate of was only about 10.1 % in neutral environments (pH 7.4). Concurrently, the course of Cu ion release from TCPP-Cu@MnO_x nanocatalyst also obtained a similar release curve of Mn ion, with 40 h of release under pH 5.0 and 10 mM GSH conditions of about 60 %, and release of 10 % in neutral conditions. In short, the above results indicated that TCPP-Cu@MnO_x nanocatalyst exhibited H^+/GSH trigger nanocatalyst continuously released metal ions (Mn and Cu), providing a possibility for ion-mediated highly toxic •OH production.

In addition, we chosen healthy BALB/c mice and randomly divided them into two groups (n = 6). Subsequently, the classified mice were injected with equal volume PBS and TCPP-Cu@MnO_x nanocatalyst (100 μL, 1 mg/mL), respectively, and the weight of mice was tracked (Fig. 4c). Analysis of kidney function, blood biochemistry, important tissue organs status (heart, liver, spleen, lung, kidney), and fluctuations in body weight showed that live toxicity and inflammation were not significant throughout the experiment (Fig. 4d, e, 4f and 4g). Subsequently, no changes such as necrosis occurred in main organs by hematoxylin and eosin (H&E) staining analysis, indicating the good biocompatibility and biosecurity (Fig. 4h).

As shown in Fig. S16, the fluorescence intensity of the tumor region increased over time after the ICG-labelled TCPP-Cu@MnO_x nanocatalyst was injected through the caudal vein 4T1 carrying mice, indicating that nano-sized nanocatalyst could be effectively enriched in the tumor sites. Furthermore, the major organs and tumors in mice were removed after 24 h. We further found that the fluorescence signal in the tumor site was the strongest compared to other organs (heart, lung, liver, spleen and kidney), demonstrating that EPR-assisted nanocatalyst accumulated at the tumor sites.

3.5. Lysosomal toxicity assessment

The over-expressed lysosomes in tumor cells have become vital target for tumor-related treatment, where the acidic properties (pH = 4.5∽5.5) [22,23] will provide an specific attack point for nanoparticle-mediated tumor therapy. Usually, the “cargo” is phagocytosed and then deliver to lysosomes, so, the escape of lysosome is a key stage in cargo-mediated treatment, especially in tumor therapy [21,26]. A large number of lysosomes appeared in tumor cells treated with TCPP-Cu@MnO_x nanocatalyst after 4 h of culture, nearly 2 times more than start group (0 h), indicating that TCPP-Cu@MnO_x nanocatalyst effectively entered into tumor cells by endocytic uptake (Fig. 5c and S17b), thereby stimulating the secretion of lysosomes in tumors [45,46]. Additionally, these similar results were also obtained for free TCPP processing group. Notably, the number ratio of lysosomes intensely diminished (2x) compared to 4 h-point as culture time increases, suggesting that acid-activated $^1O_2$-based TCPP-Cu@MnO_x nanocatalyst could effectively destroy lysosomes by liposome peroxidation (LPO) (Fig. 5a). Additionally, there was no obvious quantitative change in lysosomes of 4T1 cells treated with free TCPP for 8 h compared to 4 h of incubation, elucidating that free TCPP could be quickly eliminated *via* exocytosis or diffusion in tumor cells [47] (Fig. 5c–S17b). Interestingly, in 4 h of co-culture, 4T1 tumor cells had barely died in all processing groups, however, partial cells death occurred in TCPP-Cu@MnO_x nanocatalyst-treated group (82 %) over time compared to free TCPP group (Fig. S17a). Immediately afterwards, the apparent death was showed after 12 h of treating with TCPP-Cu@MnO_x nanocatalyst with different concentrations (10 and 50 μg/mL), while lysosomal fluorescence intensity also decreased significantly (Fig. S18). These results showed that TCPP-Cu@MnO_x nanocatalyst could effectively induce lysosomal LPO, thus triggering lysosomal-related cell death pathways (Fig. 5a).

Subsequently, TCPP-Cu@MnO_x nanocatalyst-mediated lysosomal LPO was further explored by the use of ratiometric C11-BODIPY$^{581/591}$ fluorescence probe (MKBio, China), which fluorescence shifts from red (reduction) to green (oxidation) state in the presence of lipid hydrogen peroxide (Fig. 5b). As shown in Fig. 5d and f, the untreated 4T1 cells showed prominently red fluorescence while TCPP-Cu@MnO_x nanocatalyst-treated 4T1 cells displayed the proportion of red/green fluorescence intensity decreased as concentration increases, showing that TCPP-Cu@MnO_x nanocatalyst mediated $^1O_2$ production in acidic lysosomes.

Moreover, the integrity of lysosomal subcellular organelles in 4T1 cells were further investigated by using Lysotracker green (Beyotime, China) staining experiment (Fig. 5e and g). The green fluorescence was

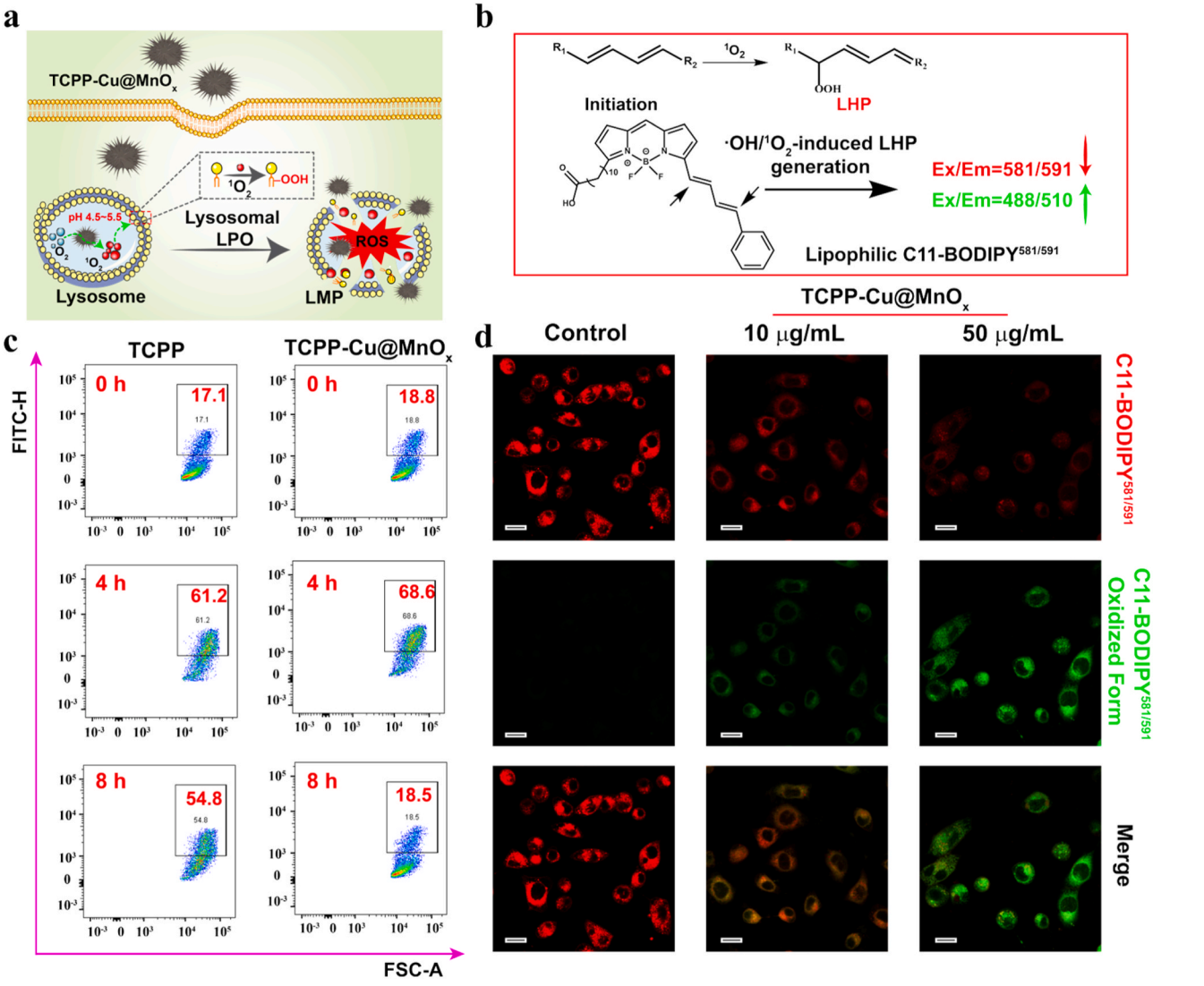

(caption on next page)

Fig. 5. TCPP-Cu@MnO_x nanocatalyst-mediated acid lysosomal LPM. (a) Schematic of proposed TCPP-Cu@MnO_x nanocatalyst-mediated acid-activated $^1O_2$ generation-mediated lysosomes damage pathways. (b) General mechanism for $^1O_2$-initiated polyunsaturated lipids containing a 1,4-pentadiene structure to the formation of lipid hydroperoxide (LHP), and proposed guidance mechanism of the lipophilic C11-BODIPY$^{581/591}$ probe of •OH/$^1O_2$ triggering for ratiometric fluorescence imaging. (c) Analysis of Lysotracker changes in 4T1 cells by flow cytometry. (d) CLSM images of C11-BODIPY$^{581/591}$-stained 4T1 cells treated with various concentrations of TCPP-Cu@MnO_x nanocatalyst for 8 h, scale bar: 20 μm. (e) CLSM images of 4T1 cells stained with Lysotracker (lysosome, green) and DAPI (nucleus, blue) after incubation with different concentrations of TCPP-Cu@MnO_x nanocatalyst (10 and 50 μg/mL) for 8 h. (f, g) The corresponding statistical analysis results *via* fluorescence intensity. Data represent mean ± standard deviation. Statistical analysis was performed by two-way ANOVA, ****$P < 0.0001$, ***$P < 0.001$.

obviously displayed in PBS-treated 4T1 cells group. However, after different concentrations TCPP-Cu@MnO_x nanocatalyst treated 4T1 cells, the green fluorescence intensity diminished and showed a dose-dependent relationship, indicating that the integrity of lysosomal membrane to be destroyed in the presence of acid-induced $^1O_2$. Importantly, $^1O_2$ induced LPO of lysosomal membrane could effectively undermine the integrity of lysosomes in tumor cells, thus promoting the release of numerous endogenous into the cytoplasm, inducing the apoptosis of cancer cells. As expected, after 12 h of co-culture, the high level of TCPP-Cu@MnO_x nanocatalyst (50 μg/mL)-managed 4T1 tumor cells clearly showed cell death and the mortality rate reached 45.7 % (Fig. S18). Conversely, 4T1 cells were alive in the presence of low concentration of TCPP-Cu@MnO_x nanocatalyst (10 μg/mL), and its survival rate was 85.8 %, compared to PBS group (survival rate of 97.9 %). Therefore, the lysosomal fluorescence intensity also displayed a concentration-dependent reduction, and has the potential to lysosomes-assisted tumor apoptosis by activating the production of ROS by acid.

3.6. Intracellular ROS levels and anticancer effect evaluation in vitro

The cytotoxicity assay of free TCPP and TCPP-Cu@MnO_x nanocatalyst were evaluated on three varieties cell lines, namely, IEC-6 cells, CT26 cells, and 4T1 cells, using the typical CCK-8 assay. As presented in Fig. 6a, TCPP or TCPP-Cu@MnO_x nanocatalyst-treated normal IEC-6 cells showed a negligible cytotoxicity at 24 h. Conversely, TCPP-Cu@MnO_x nanocatalyst-treated tumor cells (CT26 cells or 4T1 cells) showed a dose-dependent decrease in cellular vitality (Fig. 6b and c), which indicated the significant cytotoxicity *in vitro* and tumor-specific therapeutic. Moreover, free TCPP displayed non-toxic under the same treatment conditions, with a cell survival rate of 80 % even at concentration of 50 μg/mL. Suggesting that programmed activation of ROS produced of TCPP-Cu@MnO_x nanocatalyst will facilitate ROS-induced apoptosis of tumor cells.

At present, endocytosis mainly includes clathrin, caveolae/lipid raft and non-clathrin caveolin-mediated endocytosis, as well as macropinocytosis [48] to capture exogenous nanopharmaceuticals, where clathrin mediated cell phagocytosis is common. In this study, the clathrin-mediated endocytosis pathway was explored through CLSM approach. As shown in Fig. S19, the low fluorescence intensity of chlorpromazine (inhibitors of clathrin mediated endocytosis)-treated 4T1 cells was obtained, compared to the PBS group, showing that TCPP-Cu@MnO_x nanocatalyst could be ingested by clathrin manner.

Considering that TCPP-Cu@MnO_x nanocatalyst relieved the binding of intracellular lysosomes through acid-responsive ROS-induced LPO effect, resulting in the escaped "cargo" successively reacted in the cytoplasm, such as cyclic-consumption GSH by metal ions and H_2O_2-mediated ROS reactions, thereby further enhancing ROS-mediated tumor therapy. Therefore, ROS fluorescence probe, 2′,7′-dichlorofluorescin diacetate (DCFH-DA), was employed to detect the fluctuation of ROS level in cells [15,16]. As shown in Fig. 6d, there was negligible green fluorescence in PBS-treated group. Moreover, a weak fluorescence signal was observed after treating with low TCPP-Cu@MnO_x nanocatalyst concentration (10 μg/mL) in 4T1 cells, whereas when the high concentration of TCPP-Cu@MnO_x nanocatalyst (50 μg/mL) was performed in 4T1 cells, and displayed strong green fluorescence signal through CLSM imaging, demonstrating that have a potential value in tumor therapy by ROS treatment. In addition, TCPP-Cu@MnO_x nanocatalyst-treated 4T1 cells showed strong fluorescence intensity in acidic cell culture media (pH 6.5), compared to neutral condition (pH 7.4) (Fig. S20), further indicating the significant acid-activated ROS generation property.

To further differentiate ROS categories in 4T1 cells, the associated radical quenches and TCPP-Cu@MnO_x nanocatalyst were co-incubated in cell experiments. We selected NaN_3, isopropanol and benzoquinone to quench $^1O_2$, •OH and $O_2^{\bullet-}$, respectively [33], and all groups were stained with DCFH-DA probe and detected by flow analysis (Fig. S21). The study found that TCPP-Cu@MnO_x nanocatalyst treatment alone showed a higher level of ROS compared to control group, which was consistent with the above. Notably, each group of fluorescence signals decreased with the addition of quenching agents, in which quenching effect was significant by isopropanol, *i.e.*, •OH quenching, expounding that •OH-mediated ROS-based tumor therapy was the principal. Additionally, the $^1O_2$ or $O_2^{\bullet-}$ also could be produced by TCPP-Cu@MnO_x nanocatalyst, however, the yield of both ROS were secondary in 4T1 cells. Therefore, these results prove that this was consistent with the data of the TCPP-Cu@MnO_x nanocatalyst mediated ROS generation mechanisms, and again demonstrating that TCPP-Cu@MnO_x nanocatalyst was effective in producing rich ROS.

Furthermore, as the concentration of TCPP-Cu@MnO_x nanocatalyst increased, intracellular GSH levels showed a decrease in concentration correlation (Fig. 6e). The results showed that GSH-driven TCPP-Cu@MnO_x nanocatalyst decomposed the reaction and released metal ions (Mn and Cu), leading to the depletion of GSH content cycle, thereby destroying the oxidation balance and enhancing the therapeutic effect.

Intuitively, TCPP-Cu@MnO_x nanocatalyst treated 4T1 cells to determine live/dead in cells through calcein-AM/propidium iodide (PI) staining assay, in which calcein-AM dye stains the living cells green and the dead cells appears red by PI dye (Fig. 6f). The concentration-dependent death pattern of TCPP-Cu@MnO_x nanocatalyst were demonstrated, with the highest red fluorescence content at 50 μg/mL dose. Subsequently, we also evaluated apoptosis of TCPP-Cu@MnO_x nanocatalyst with diverse concentrations using the Annexin V-FITC apoptosis detection kit. As shown in Fig. 6g, the apoptosis rate of TCPP-Cu@MnO_x nanocatalyst was dose-dependent, and these outcomes were consistent with the *in vitro* cytotoxicity assays, implying that TCPP-Cu@MnO_x nanocatalyst could effectively kill tumor cells through inducing ROS generation.

3.7. Antitumor study in vivo

The therapeutic effects of TCPP-Cu@MnO_x nanocatalyst mediated 4T1-bearing tumor mice were further assessed on the basis of the above evidence (normal cell resistance, tumor cytotoxicity and biosafety). After the establishment of the 4T1-bearing tumor models, the classified mice ($n = 5$) were intravenously injected with equal volume of PBS (control, 100 μL) and different doses TCPP-Cu@MnO_x nanocatalyst (2.5 mg/kg and 5 mg/kg), and dosage frequency was once every two days, with a total of three doses administered throughout the course of 27 days treatment (Fig. 7a). All mice were recorded and computed in real time including mouse weight and tumor-bearing volume. The tracking document showed no obvious weight changes in all mice with 4T1 tumor after treatment (Fig. 7c), suggesting the significant biosecurity. As expected, the volumes of tumor showed time and concentration-dependent reduction in TCPP-Cu@MnO_x nanocatalyst treatment, compared to control group (PBS treatment) (Fig. 7b), indicating that TCPP-Cu@MnO_x nanocatalyst could effectively inhibit tumor growth by

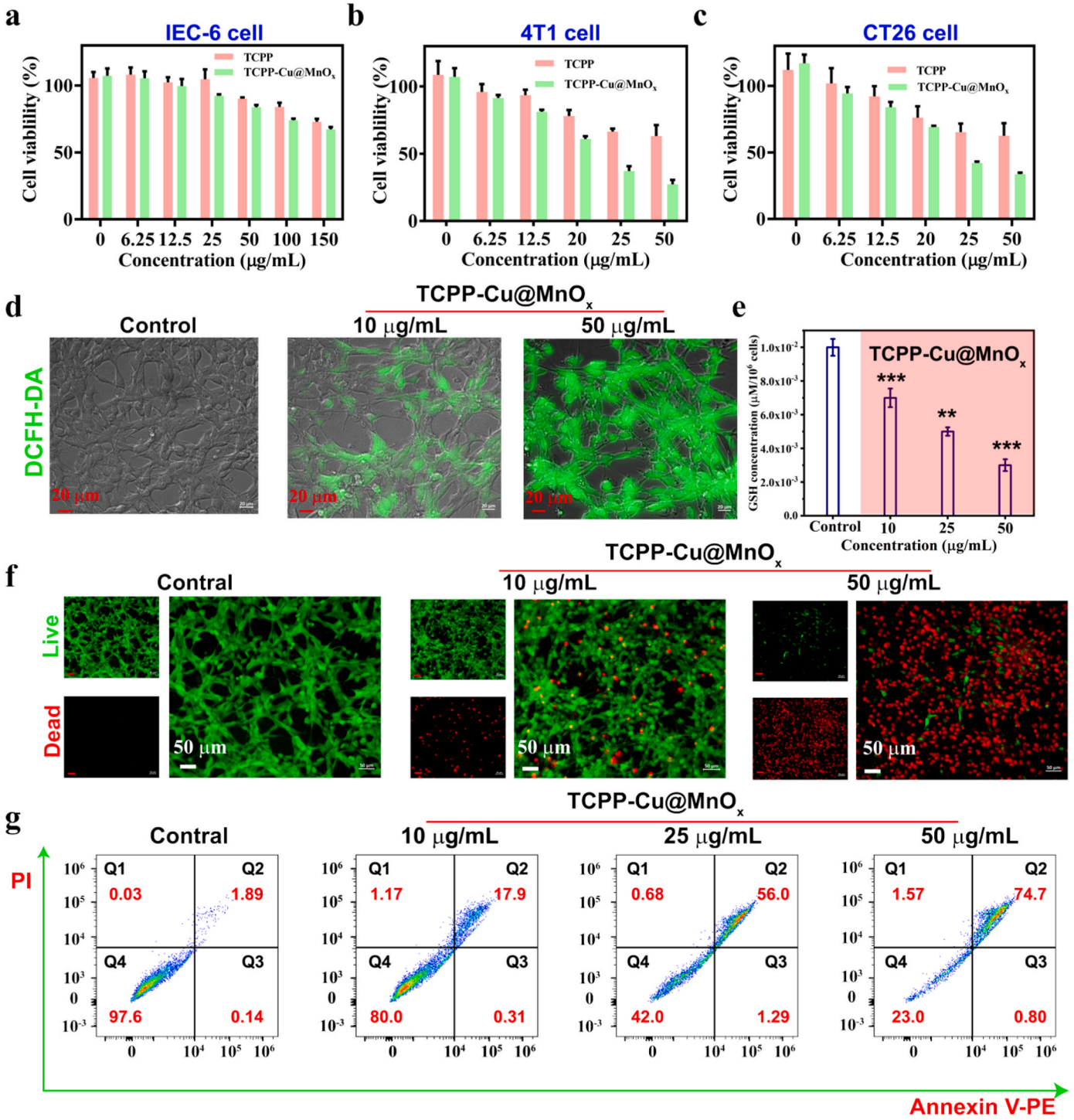

Fig. 6. Assessment of cytotoxicity *in vitro*. (a) Cell viability of IEC-6 cells (a), 4T1 cells (b) and CT26 cells (c) after incubation with TCPP-Cu@MnO_x nanocatalyst and free TCPP at elevated concentrations (0, 6.25, 12.5, 20, 25, and 50 μg/mL) for 24 h. (d) Fluorescence imaging of 4T1 cells stained with DCFH-DA, scale bar = 50 μm. (e) Testing of intracellular GSH levels. (f) Fluorescence imaging of 4T1 cells by live-dead cell staining assay (PI (red fluorescence) and calcein-AM (green fluorescence)) after different treatments. (g) Flow-cytometry apoptosis assay of 4T1 cells after incubation with different doses of TCPP-Cu@MnO_x nanocatalyst followed by staining with Annexin-FITC and PI. Data represent mean ± standard deviation. Statistical analysis was performed by two-way ANOVA, ***P < 0.0001, **P < 0.01, *P < 0.05.

programming the production of ROS. Next, all mice were sacrificed, and tumors and important organs (heart, liver, spleen, lung, kidney) were collected and analyzed. The photograph of tumor (Fig. 7e) and tumor weight (Fig. 7d) displayed the smallest size after high-dose treating (5 mg/kg), with similar results to tumor growth curves. To in-depth understanding the therapeutic efficacy of TCPP-Cu@MnO_x nanocatalyst, H&E, TdT-mediated dUTP nickend labeling (TUNEL) and Ki-67 antibody staining of tumor tissues were conducted. The diversity in cellular status in PBS-treated group was insignificant. Comparatively, H&E and TUNEL results showed concentration-correlated dead cells in TCPP-Cu@MnO_x nanocatalyst-managed tumor sections (Fig. 7f–S22). Additionally, Ki-67 antibody staining as an important indicator tumor

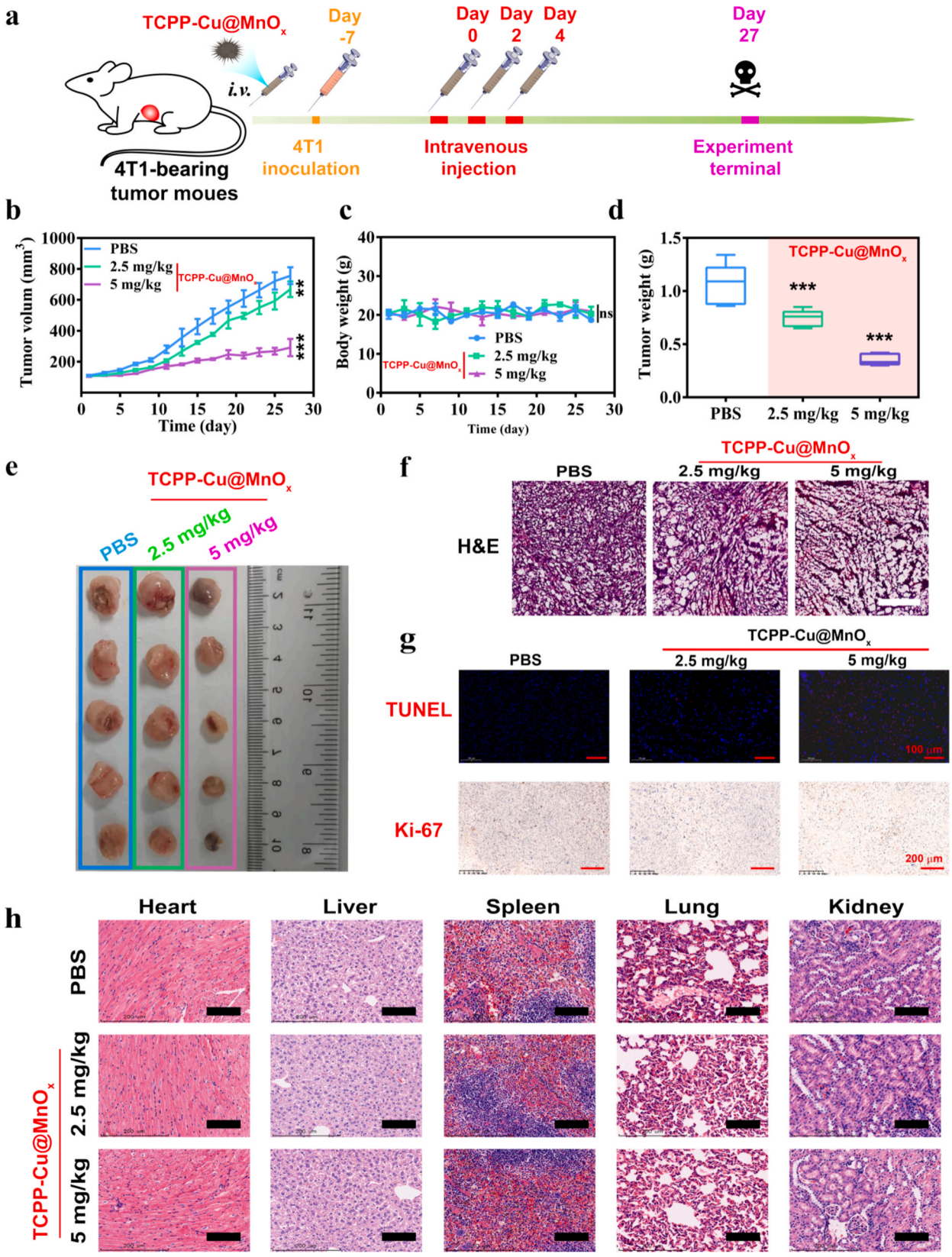

Fig. 7. Evaluation of antitumor efficacy of TCPP-Cu@MnO_x nanocatalyst in vivo. (a) Schematics illustration on TCPP-Cu@MnO_x nanocatalyst for the treatment of 4T1 tumor mice. (b) Tumor growth curves of all treated groups. (c) Body weight of mice throughout the therapeutic processes. (d) Weights of collected tumors at day 27. (e) Images of tumor obtained from 4T1-bearing BALB/c mice after 27 days of treatment. (f) H&E staining images of tumors, scale bar: 100 μm. (g) TUNEL and Ki-67 staining in tumor region of each group after treatment with TCPP-Cu@MnO_x nanocatalys. (h) Representative H&E stained major organ tissue sections of groups, scale bar: 100 μm. Data represent mean ± standard deviation. Statistical analysis was performed by two-way ANOVA, ***P < 0.001, **P < 0.01, *P < 0.05, ns: no significant.

proliferative status were detected, and their results were in accordance with H&E and TUNEL results, further confirming that programmed activation of ROS of TCPP-Cu@MnO_x nanocatalyst could effectively drive coordinated amplification therapy in tumor.

Furthermore, after varied treatments, biosafety and organ damage of 4T1-bearing tumor mice were investigated by blood/renal routine as well as H&E staining of major organs (heart, liver, spleen, lung, and kidney). No obvious pathological changes in tissues were observed by H&E staining (Fig. 7e), and the parameters of blood/renal routine were normal and no inflammation occurred, indicating the relatively high therapeutic biosafety (Fig. S23).

4. Conclusions

Limited efficiency of ROS production (insufficient supply of H_2O_2 and low catalytic capacity, *etc.*) and the effect of lysosomal retention in tumor cells will heavily hinder the treatment of tumor. Therefore, intelligent TCPP-Cu@MnO_x nanocatalyst ($(Mn^{II})_1(Mn^{III})_{2.1}(Mn^{IV})_{2.6}O_{9.35}$) was constructed in this work, for enhanced ROS-based therapy against tumors, which displayed significant stability, TME-responsive degradation behaviors, as well as catalytic functions. More important, the acidity-unlocked bioreactor TCPP-Cu@MnO_x nanocatalyst exhibited an *in situ* unsolicited triggering of abundant $^1O_2$ generation to mediate lysosomal damage by $^1O_2$ inducing LMP, meanwhile, disrupted the integrity of lysosomes, causing nanocatalyst to escape and kill tumor cells. Subsequently, TCPP-Cu@MnO_x nanocatalyst was effectively captured by reducing substance of GSH, causing its degradation and apparent consumption of endogenous GSH in cytoplasm. Additionally, based on Fenton-like reaction and TCPP-mediated peroxide derivatives reaction, abundant ROS (•OH and $^1O_2$) with high cytotoxicity were obtained by endogenous H_2O_2-medaited the release of Mn/Cu ions, then, further effectively inducing tumor cells death. Thus, the strategy of programmed ROS enhancement-mediated tumor ablation has been proposed, which will provide a new window for ROS-based tumor therapy.

CRediT authorship contribution statement

Mingliang Pei: Writing – review & editing, Writing – original draft, Visualization, Validation, Supervision, Software, Resources, Project administration, Methodology, Investigation, Funding acquisition, Formal analysis, Data curation, Conceptualization. **Xin Guan:** Project administration, Methodology, Investigation, Formal analysis, Data curation, Conceptualization. **De Zhao:** Data curation, Formal analysis, Funding acquisition, Investigation, Methodology. **Fan Yang:** Methodology, Investigation, Formal analysis, Data curation. **Yun Dong:** Methodology, Investigation, Formal analysis, Data curation, Conceptualization. **Manxiu Huai:** Software, Project administration, Methodology, Investigation, Formal analysis, Data curation. **Wensong Ge:** Methodology, Investigation, Data curation. **Xiaodong Hou:** Software, Investigation, Formal analysis, Data curation. **Wenfeng Chu:** Methodology, Investigation, Formal analysis, Data curation. **Kai Wang:** Methodology, Investigation, Data curation. **Jie Chen:** Validation, Software, Project administration, Investigation, Funding acquisition, Formal analysis, Data curation. **Huixiong Xu:** Validation, Supervision, Resources, Project administration, Investigation, Funding acquisition, Formal analysis, Conceptualization.

Declaration of competing interest

The authors declare no competing interests.

Acknowledgements

This work was supported by China Postdoctoral Science Foundation (2021M692433), Shanghai Post-Doctoral Excellence Program (2020408), Natural projects for basic research of Shanghai Chest Hospital (2020YNJCQ12), Science and Technology Commission of Shanghai Municipality Scientific and Innovative Action Plan of Shanghai (CN) (21142202200), and the Youth Program of National Natural Science Foundation of China (82102049).

Appendix A. Supplementary data

Supplementary data to this article can be found online at https://doi.org/10.1016/j.mtbio.2024.101299.

Data availability

The data that has been used is confidential.

References

[1] D. Kalyane, D. Choudhary, S. Polaka, H. Goykar, T. Karanwad, K. Rajpoot, R. K. Tekade, Reactive oxygen nano-generators for cancer therapy, Prog. Mater. Sci. 130 (2022) 100974.
[2] H. Yang, R.M. Villani, H. Wang, M.J. Simpson, M.S. Roberts, M. Tang, X. Liang, The role of cellular reactive oxygen species in cancer chemotherapy, J. Exp. Clin. Cancer Res. 37 (2018) 266.
[3] L. Zhang, C.X. Li, S.S. Wan, X.Z. Zhang, Nanocatalyst-mediated chemodynamic tumor therapy, Adv. Healthcare Mater. 11 (2022) 2101971.
[4] X. Wang, X. Zhong, Z. Liu, L. Cheng, Recent progress of chemodynamic therapy-induced combination cancer therapy, Nano Today 35 (2020) 00946.
[5] L. Huang, S. Zhao, J. Wu, L. Yu, N. Singh, K. Yang, M. Lan, et al., Photodynamic therapy for hypoxic tumors: advances and perspectives, Coordin. Chem. Rev. 438 (2021) 213888.
[6] L. Dong, W. Li, Yu Luo, C. Liu, K. Li, Y. Chen, G. Hong, Engineering molybdenum-assisted tellurium nanosonosensitizers for enhanced sonodynamic tumor nanotherapy, Adv. Funct. Mater. 33 (2023).
[7] M. Zhang, L. Dong, D. Li, L. Zhu, R. Peng, X. Liu, K. Wang, X. Wang, Y. Zhu, H. Sun, Y. Luo, Sonocatalytic in situ induced oxygen storm precision enhanced reactive oxygen therapy for pancreatic cancer, Adv. Funct. Mater. 33 (2023).
[8] R. Fisher, L. Pusztai, C. Swanton, Cancer heterogeneity: implications for targeted therapeutics, Br. J. Cancer 108 (2013) 479–485.
[9] C. Fedele, R.W. Tothill, G.A. McArthur, Navigating the challenge of tumor heterogeneity in cancer therapy, Cancer Discov. 4 (2014) 146–148.
[10] J. Yang, H. Yao, Y. Guo, B. Yang, J. Shi, Enhancing tumor catalytic therapy by co-catalysis, Angew. Chem. Int. Ed. Engl. 61 (2022) e202200480.
[11] Y. Li, R. Jia, H. Lin, X.L. Sun, F. Qu, Synthesis of $MoSe_2/CoSe_2$ nanosheets for NIR-enhanced chemodynamic therapy via synergistic in-situ H_2O_2 production and activation, Adv. Funct. Mater. 31 (2021) 2008420.
[12] W. Cao, M. Jin, K. Yang, B. Chen, M. Xiong, X. Li, G. Cao, Fenton/Fenton-like metal-based nanomaterials combine with oxidase for synergistic tumor therapy, J. Nanobiotechnol. 19 (2021) 325.
[13] J. Xiao, G. Zhang, R. Xu, H. Chen, H. Wang, G. Tian, B. Wang, C. Yang, et al., A pH-responsive platform combining chemodynamic therapy with limotherapy for simultaneous bioimaging and synergistic cancer therapy, Biomaterials 216 (2019) 119254.
[14] L.S. Lin, T. Huang, J. Song, X.Y. Ou, Z. Wang, et al., Synthesis of copper peroxide nanodots for H_2O_2 self-supplying chemodynamic therapy, J. Am. Chem. Soc. 141 (2019) 9937–9945.
[15] Y. Han, J. Ouyang, Y. Li, F. Wang, J.H. Jiang, Engineering H_2O_2 self-supplying nanotheranostic platform for targeted and imaging-guided chemodynamic therapy, ACS Appl. Mater. Inter. 12 (2020) 288–297.
[16] M. Zhang, B. Shen, R. Song, H. Wang, B. Lv, X. Meng, Y. Liu, et al., Radiation-assisted metal ion interference tumor therapy by barium peroxide-based nanoparticles, Mater. Horiz. 6 (2019) 1034–1040.
[17] D.H. Zhao, C.Q. Li, X.L. Hou, X.T. Xie, B. Zhang, G.Y. Wu, et al., Tumor microenvironment-activated theranostics nanozymes for fluorescence imaging and enhanced chemo-chemodynamic therapy of tumors, ACS Appl. Mater. Inter. 13 (2021) 55780–55789.
[18] Z. Ren, S. Sun, R. Sun, G. Cui, L. Hong, B. Rao, A. Li, Z. Yu, Q. Kan, Z. Mao, Metal-polyphenol-coordinated nanomedicine for synergistic cascade cancer chemotherapy and chemodynamic therapy, Adv. Mater. 32 (2020) 1906024.
[19] S.L. Li, P. Jiang, F.L. Jiang, Y. Liu, Recent advances in nanomaterial-based nanoplatforms for chemodynamic cancer therapy, Adv. Funct. Mater. 31 (2021) 2100243.
[20] X. Tian, A. Shi, H. Yin, Y. Wang, Q. Liu, W. Chen, J. Wu, Nanomaterials respond to lysosomal function for tumor treatment, Cells 11 (2022) 3348.
[21] J. Pu, C.M. Guardia, T. Keren-Kaplan, J.S. Bonifacino, Mechanisms and functions of lysosome positioning, J. Cell Sci. 129 (2016) 4329–4339.
[22] P. Saftig, J. Klumperman, Lysosome biogenesis and lysosomal membrane proteins: trafficking meets function, Nat. Rev. Mol. Cell Biol. 10 (2009) 623–635.
[23] L.K.K. Holland, I.Ø. Nielsen, K. Maeda, M. Jäättelä, SnapShot: lysosomal functions, Cell 181 (2020) 748–748.e1.

[24] H. Wang, H. Zhang, Y. Xiang, W. Pan, N. Li, B. Tang, An efficient strategy for cancer therapy using a tumor- and lysosome-targeted organic photothermal agent, Nanoscale 13 (2021) 8790–8794.
[25] S. Ji, J. Li, X. Duan, J. Zhang, Y. Zhang, M. Song, S. Li, H. Chen, D. Ding, Targeted enrichment of enzyme-instructed assemblies in cancer cell lysosomes turns immunologically cold tumors hot, Angew. Chem. Int. Ed. Engl. 60 (2021) 26994–27004.
[26] W. Huang, Y. Zhang, X. Tan, N. Wang, J. Wang, M. He, J. Peng, J. Hu, et al., An AIEgen-based photosensitizer for lysosome imaging and photodynamic therapy in tumor, Sens. Actuators B: Chem. 335 (2021) 129698.
[27] L. Yang, E. Bracho-Sanchez, L.P. Fernando, J.S. Lewis, M.R. Carstens, C.L. Duvall, B.G. Keselowsky, Poly(2-propylacrylic acid)/poly(lactic-co-glycolic acid) blend microparticles as a targeted antigen delivery system to direct either $CD4^+$ or $CD8^+$ T cell activation, Bioeng. Transl. Med. 2 (2017) 202–211.
[28] S. Roy, D. Zhu, W.J. Parak, N. Feliu, Lysosomal proton buffering of poly (ethylenimine) measured in situ by fluorescent pH-sensor microcapsules, ACS Nano 14 (2020) 8012–8023.
[29] R. Wang, C. Yin, C. Liu, Y. Sun, P. Xiao, J. Li, S. Yang, W. Wu, X. Jiang, Phenylboronic acid modification augments the lysosome escape and antitumor efficacy of a cylindrical polymer brush-based prodrug, J. Am. Chem. Soc. 143 (2021) 20927–20938.
[30] C.G. Liu, H.X. Tang, X. Zheng, D.Y. Yang, Y. Zhang, J.T. Zhang, R.K. Kankala, et al., Near-infrared-activated lysosome pathway death induced by ROS generated from layered double hydroxide-copper sulfide nanocomposites, ACS Appl. Mater. Inter. 12 (2020) 40673–40683.
[31] G. He, N. Xu, H. Ge, Y. Lu, R. Wang, H. Wang, J. Du, J. Fan, W. Sun, et al., Red-light-responsive Ru complex photosensitizer for lysosome localization photodynamic therapy, ACS Appl. Mater. Inter. 13 (2021) 19572–19580.
[32] H. Deng, Z. Yang, X. Pang, C. Zhao, J. Tian, Z. Wang, X. Chen, Self-sufficient copper peroxide loaded pKa-tunable nanoparticles for lysosome-mediated chemodynamic therapy, Nano Today (2022) 101337.
[33] C. Wang, F. Cao, Y. Ruan, X. Jia, W. Zhen, X. Jiang, Specific generation of singlet oxygen through the Russell mechanism in hypoxic tumors and GSH depletion by Cu-TCPP nanosheets for cancer therapy, Angew. Chem. Int. Ed. 58 (2019) 9846.
[34] S. Belal, O. Abdel-Razak, A.F. El-Walily, R. Bakry, Spectrophotometric determination of captopril and penicillamine through the use of ligand exchange complexation reactions, Int. J. Biomed. Sci. 7 (2011) 289–294.
[35] B. Zhuang, X. Li, R. Ge, S. Kang, L. Qin, G. Li, Assembly and electron transfer mechanisms on visible light responsive 5,10,15,20-meso-tetra(4-carboxyphenyl) porphyrin/cuprous oxide composite for photocatalytic hydrogen production, Appl. Catal. A: Gen. 533 (2017) 81–89.
[36] Z. Zhao, S. Dong, Y. Liu, J. Wang, L. Ba, C. Zhang, X. Cao, et al., Tumor microenvironment-activable manganese-boosted catalytic immunotherapy combined with PD-1 checkpoint blockade, ACS Nano 16 (2022) 20400–20418.
[37] B. Ding, P. Zheng, F. Jiang, Y. Zhao, M. Wang, M. Chang, P.'a. Ma, J. Lin, MnO_x nanospikes as nanoadjuvants and immunogenic cell death drugs with enhanced antitumor immunity and antimetastatic effect, Angew. Chem. Int. Ed. 59 (2020) 16381.
[38] M. Pei, X. Jia, X. Zhao, J. Li, P. Liu, Alginate-based cancer-associated, stimuli-driven and turn-on theranostic prodrug nanogel for cancer detection and treatment, Carbohydr. Polym. 183 (2018) 131–139.
[39] M. Pei, G. Li, P. Liu, Tumor-specific fluorescent Cdots-based nanotheranostics by acid-labile conjugation of doxorubicin onto reduction-cleavable Cdots-based nanoclusters, Mater. Sci. Eng. C (2020) 110719.
[40] B. Ding, P. Zheng, J. Tan, H. Chen, Y. Bian, C. Yang, P. Ma, J. Lin, Pyroptosis adjuvants: gram-scale production, cascade catalysis, and in situ antitumor immunity activation, Chem. Mater. 34 (2022) 1800–1808.
[41] S. Lu, W. Feng, X. Yao, X. Song, J. Guo, Y. Chen, Z. Hu, Microorganism-enabled photosynthetic oxygeneration and ferroptosis induction reshape tumor microenvironment for augmented nanodynamic therapy, Biomaterials 287 (2022) 121688.
[42] Q. Zhang, Q. Luo, Z. Liu, M. Sun, X. Dong, Nano-ROS-generating approaches to cancer dynamic therapy: lessons from nanoparticles, Chem. Eng. J. 457 (2023) 141225.
[43] D. Ding, Y. Feng, R. Qin, S. Li, L. Chen, J. Jing, C. Zhang, et al., Mn^{3+}-rich oxide/persistent luminescence nanoparticles achieve light-free generation of singlet oxygen and hydroxyl radicals for responsive imaging and tumor treatment, Theranostics 11 (2021) 7439–7449.
[44] C. Lu, C. Zhang, P. Wang, Y. Zhao, Y. Yang, Y. Wang, H. Yuan, et al., Light-free generation of singlet oxygen through manganese-thiophene nanosystems for pH-responsive chemiluminescence imaging and tumor therapy, Chem 6 (2020) 2314–2334.
[45] W. Ma, H. Zhang, S. Li, Z. Wang, X. Wu, R. Yan, F. Geng, W. Mu, Y. Jin, A multifunctional nanoplatform based on Fenton-like and Russell reactions of Cu, Mn bimetallic ions synergistically enhanced ROS stress for improved chemodynamic therapy, ACS Biomater. Sci. Eng. 8 (2022) 1354–1366.
[46] X. Luan, Y. Pan, Y. Zhou, D. Zhou, W. Zhao, F. Zeng, Z. Zhu, Q. Lu, et al., Targeted self-assembly of renal clearable $Cu_{2-x}Se$ to induce lysosome swelling for multimodal imaging guided photothermal/chemodynamic synergistic therapy, Adv. Funct. Mater. 32 (2022) 2208354.
[47] M. Borkowska, M. Siek, D.V. Kolygina, Y.I. Sobolev, S. Lach, S. Kumar, et al., Targeted crystallization of mixed-charge nanoparticles in lysosomes induces selective death of cancer cells, Nat. Nanotechnol. 15 (2020) 331–341.
[48] J. Chen, C. Fang, C. Chang, K. Wang, H. Jin, T. Xu, J. Hu, W. Wu, E. Shen, K. Zhang, Ultrasound-propelled liposome circumvention and siRNA silencing reverse BRAF mutation-arised cancer resistance to trametinib, Colloids Surf., B 234 (2024) 113710.